QUANTIFYING THE EFFECTS OF KNEE JOINT BIOMECHANICS ON ACOUSTICAL EMISSIONS

A Dissertation
Presented to
The Academic Faculty

by

Hyeon Ki Jeong

In Partial Fulfillment
of the Requirements for the Degree
Doctor of Philosophy in the
School of Electrical and Computer Engineering

Georgia Institute of Technology
August 2021

QUANTIFYING THE EFFECTS OF KNEE JOINT BIOMECHANICS ON ACOUSTICAL EMISSIONS

Approved by:

Dr. Omer Inan, Advisor
School of Electrical and Computer Engineering
Georgia Institute of Technology

Dr. Thomas Ploetz
School of Interactive Computing
Georgia Institute of Technology

Dr. Aaron Young
School of Mechanical Engineering
Georgia Institute of Technology

Dr. Mindy L. Millard-Stafford
School of Biological Sciences
Georgia Institute of Technology

Dr. Farrokh Ayazi
School of Electrical and Computer Engineering
Georgia Institute of Technology

ACKNOWLEDGEMENT

It has been a long journey ever since I first joined the lab as an undergraduate researcher. The years of my PhD journey can be summarized as perseverance, gratitude, and more importantly friendship.

I had the privilege to work with Dr. Omer Inan, whom I can call a mentor, an advisor, a friend, and an inspirer. He offered many guidance, technical assistance, supervision, and moral support. I first met him as an undergraduate student and his vision and energy indeed allowed me to diverge into one of the challenging problems and inspired my scientific education. He has been a true leader and create the atmosphere for the students to dive into the field of biomedical research knowing that he was there to support us through the journey. He led by example and showed great work ethic. I can say it has been my honor to work alongside with him and I want to thank him for being a friend, a mentor, and last but not least, a great leader.

I would like to extend my thanks to all members of my committee: Dr. Aaron Young, Dr. Farrokh Ayazi, Dr. Thomas Ploetz, and Dr. Melinda Millard-Stafford. I truly appreciate the constructive feedbacks and discussions to help me think through problems.

I am truly grateful to be part of the research group that shared many laughs, talks, discussions, and friendship. I would like to thank my colleagues: Samer Mabrouk, Nordine Sebkhi, Oludotun Ode, Hewon Jung, Venu Ganti, Jacob Kimball, Goktug Ozmen, Luis Rosa, Sungtae An, Sevda Gharehbaghi, Asim Gazi, Kristy Scott, David Lin, Arpan Bhavsar, Keaton Scherpereel, Camille Johnson, Anna Harrison, Antonio Sanchez Perez,

Mohammad Nikbakht, Michael Chan, John Berkebile, Christopher Nichols, Emily Moise, Tamara Lambert, Adith Srivatsa. I would also like to thank former lab members, Dr. Hakan Toreyin, Jordan Conant, Dr. Maziyar Pouyan, Dr. Hazar Ashouri, Dr. Ozan Bicen, Dr. Daniel Whittingslow, Dr. Andrew Carek, Dr. Sinan Hersek, Dr. Yaoyao Jia, Dr. Caitlin Teague, Dr. Nick Bolus, Dr. Jon Zia, Dr. Nil Gurel, Dr. Mohsen Safaei, Brandi Nevius, Dr. Mobashir Shandhi, and Daniel Hochman. Especially, I would like to thank Venu, Hewon, Samer, and Daniel for being a true friend with numerous discussions throughout the years and a person to go to for casual talks whenever we felt stressed from the work. I would like to thank Nick and Mohsen for being a great friend and a mentor regarding my PhD work and inspiring me with ideas.

I would also like to thank my friends both in graduate years and undergraduate years in making Atlanta my second home. I would like to thank my friends from Korea whom I chat with every now and then but always with laughter.

I would like to thank my girlfriend, Seulji, for supporting me throughout my PhD journey. She has been on my side both good and bad time and always believed in me. The words cannot describe how grateful I am and I am looking forward to how our life will grow together.

I also want to thank my parents and my brother for being a tremendous support throughout my life. They have dedicated their life and provided me with endless support to allow me to pursue my dreams and goals. Without the endless love, guidance and support from my parents, I would not be here. They are always the source of my strength and motivation.

TABLE OF CONTENTS

LIST OF TABLES

LIST OF FIGURES

LIST OF SYMBOLS AND ABBREVIATION

ACL	Anterior Cruciate Ligament
ANOVA	Analysis of Variance
AUC	Area Under Curve
BW	Body Weight
CAE	Convolutional Autoencoder
CEINMS	Calibrated EMG-informed Neuromusculoskeletal Modelling
CNN	Convolutional Neural Network
DAQ	Data Acquisition
EMG	Electromyography
FFT	Fast Fourier Transform
GCF	Graph Community Factor
GRF	Ground Reaction Force
IMU	Inertial Measurement Unit
IRB	Institutional Review Board
JAE	Joint Acoustic Emission
JCF	Joint Contact Force
kNN	k-Nearest Neighbor
LOSO-CV	Leave one subject-out cross validation
MCL	Medial Collateral Ligament
MFCC	Mel-frequency Cepstrum Coefficient
MSE	Mean Squared Error
MSKM	Musculoskeletal Modeling

MRI	Magnetic Resonance Imaging
OA	Osteoarthritis
PCL	Posterior Cruciate Ligament
STFT	Short Time Fourier Transform
SVM	Support Vector Machine
TFCF	Tibiofemoral Contact Force
TKA	Total Knee Arthroplasty
t-SNE	t-stochastic Neighbor Embedding
UMAP	Uniform Manifold Approximation and Projection

SUMMARY

The knee is one of the most injured body parts, causing 18 million patients to be seen in clinics every year [1]. Because the knee is a weight bearing joint, it is prone to pathologies such as osteoarthritis and ligamentous injuries. Existing technologies for monitoring knee health can provide accurate assessment and diagnosis for acute injuries. However, they are mainly confined to clinical or laboratory settings only, time-consuming, expensive, and not well-suited for longitudinal monitoring. Developing a novel technology for joint health assessment beyond the clinic can further provide insights on the rehabilitation process and quantitative load of the knee joint.

The objective of this research is to investigate joint acoustic emissions (JAEs) from joint movements as a potential biomarker for longitudinal monitoring and explore novel methods of interpreting the characteristics of the JAEs especially in relation to knee joint load. First, we developed a novel processing technique for JAEs that quantify on the structural change of the knee from injured athletes and human lower-limb cadaver models. Second, we quantified whether JAEs can detect the increase in the mechanical stress on the knee joint using an unsupervised graph mining algorithm. Lastly, we quantified the directional bias of the load distribution between medial and lateral compartment using JAEs. Understanding and monitoring the quantitative usage of knee loads in daily activities can broaden the implications for longitudinal joint health monitoring.

CHAPTER 1. INTRODUCTION

1.1 Motivation

The knee is one of the most complex joints with several anatomical planes of articulation with large [2], multidirectional stresses put on the knee during movement, making it prone to factures, sprains, tears, dislocations and is one of the most frequently injured body parts—especially in athletes [3]. Diagnosing and monitoring knee health is a viable target for innovation especially, but existing technologies are mainly confined to clinical or laboratory settings such as medical imaging [4] and biomechanics instrumentation [5]. While these technologies provide great value in facilitating one-time assessments like those needed for acute injury diagnosis [6], they are not well-suited for monitoring the rehabilitation of the injury. For example, repeat MRIs are time intensive, confined to a clinical setting, difficult to schedule, and cost prohibitive – particularly for underserved populations. Thus, there is a compelling need for enabling continuous knee health sensing using inexpensive technologies that provide in-depth physiology and functional information. Wearable knee health sensing technologies could benefit those suffering from joint injury by providing easily interpretable feedback on rehabilitation progress and perhaps even provide warnings before injuries occur and allow longitudinal monitoring outside of a clinical or laboratory settings.

The idea of capturing acoustical emissions from the knee has been explored previously as a means of diagnosing and differentiating between healthy and impaired knee joints. Previous work has shown that acoustic emissions captured from arthritic knees are different than the signals captured from the healthy knees [7-9]. These findings

demonstrate the viability of using these signals as a tool for noninvasive diagnosis and monitoring of cartilage pathology. One aspect that is of clinical interest is the quantification of knee joint loads throughout daily living activities and exercises. Prior work in estimating knee loading forces has been constrained to a laboratory setting using biomechanics toolbox or from the force sensors instrumented in the total knee replacement or knee prothesis [10-12]. However, quantification knee joint loading using a potential wearable sensing has never been previously demonstrated.

To better understand the underlying properties and fundamentals of joint sounds, this research will investigate the relationship between the changes in the knee joint structure (i.e. structural damage and joint contact force) and the JAEs while developing novel techniques for analyzing these sounds. We envision that the possibility of quantifying joint structure and joint load usage from these acoustic sensors would advance the potential of JAE as the next biomarker of joint health that can be captured with wearable technology.

1.2 Major Contributions of this Work

Knee acoustic emissions have been previously studied as a potential biomarker for evaluating joint health. To the best of our knowledge, no work has focused on translating these acoustic data for longitudinal monitoring or quantifying joint contact force that would potentially provide insights to the knee usage and cartilage health during daily activities and drive future projects. As such, the major contribution of this work include:

1) Quantified the specific characteristics of JAEs that correspond to structural damage using both cadaver models and in vivo studies for potential longitudinal assessment.

2) Discovered, for the first time, that JAEs can quantify the increase in the mechanical stress of the knee using an unsupervised clustering algorithm via graph mining.
3) Demonstrated that JAEs can determine the directional bias of medial to lateral load distribution by using representation learning via convolutional autoencoder in a subject independent model.

1.3 Dissertation Organization

The remainder of this dissertation is organized as follows: In Chapter 2, a brief background of JAE and previous signal processing methods from the literature are presented. Then, a novel method for longitudinal joint health assessment is introduced and validated on datasets acquired from athletes with acute injuries at the time of the injury followed by 4-6 months of post-recovery phase and an injury model in human lower limb cadavers. Chapter 3 explores a novel method to quantify whether the characteristics of acoustical emissions from the joint change in response to the increased biomechanical stress on the joint using an unsupervised graph mining technique. This methods extracts the number of complex communities to determine the heterogeneity of the sounds as the joints experience greater mechanical stress. Chapter 4 demonstrates that knee acoustics can detect the directional bias of medial to lateral joint load distribution by using automated feature extraction and sensor fusion algorithms. Finally, in chapter 5, the conclusions, impact, and directions for future work are discussed.

CHAPTER 2. NOVEL METHODS FOR PROCESSING JOINT ACOUSTIC EMISSION

2.1 Introduction

In this chapter, a brief background of various signal processing methods for JAEs is first presented. Then, a novel method of analyzing JAE and the result of estimating joint health using the proposed technique from the dataset acquired after acute injury and post recovery in athletes and from cadaver legs at four different stages of intervention are presented. The methods presented are not limited to classifying health versus injured knee status but provides the possibility of using JAE as a potential longitudinal assessment tool.

2.2 Joint Acoustic Emissions

JAEs has been studied as a potential biomarker for quantifying knee joint health. The joint sounds generally occur when anatomical structures are in contact with each other during movement which could capture information regarding the changes in the physiological structure of the joint. The idea of joint sounds as a marker of health has first been reported in 1902 when Blodgett used a stethoscope and reported that auscultation of the knee joint could serve as a potential diagnostic tool [7]. Over the past century, researchers have investigated these joint sounds to distinguish healthy knees from those with degenerative diseases or injuries using surface vibration sensors (e.g. accelerometers, piezoelectric devices, and stethoscope) or “air” microphones (e.g. microelectromechanical systems and electret microphones). The air microphones will measure attenuated, higher frequency signals and have less of motion artifact. Accelerometers, on the other hand,

directly measure the original non-attenuated signals and have less sensitivity to the background noise. The sensors will measure the JAEs produced during joint articulation and these signals are processed using signal processing techniques.

Because the knee is one of the largest and most complex joint in the body consisting of diverse anatomical mechanisms, the exact origin of the joint acoustics is difficult to quantify. The most common cause of the pathological JAEs would be the cartilage degenerations leading to osteoarthritis (OA) which is known to be the eleventh largest cause of disability and the sixth largest cause of mobility impairment [13]. Injuries such as lesions of ligaments, distortions, cartilage lesions, contusions, and dislocations could develop OA [3] and result in physiological changes of the tissue such as softening or loss of cartilage [14]. Shark et al. investigated the OA knees and concluded that OA knees produce higher peaks, longer duration, and more frequent acoustical emissions than the healthy knees [8]. Prior et al studied the high frequency component of the OA knees and discovered that OA knees had more joint acoustical events, defined as burst signal waveforms above a threshold of 32 dB [9]. Many of the previous studies have sought to develop acoustical processing technique to classify subjects, most often as either healthy or injured knees [15-17]. Few studies have focused on differentiating the types and severity of knee joint cartilage pathology, or the location of injuries [18, 19].

2.2.1 Signal Processing and Feature Extraction of Joint Acoustical Emissions

Many of the prior cross-sectional studies on knee JAEs have been successful in distinguishing healthy versus injured knees. However, the types of features and classification methods still differ and there are no gold standard metrics for quantifying the

characteristics of the JAEs. The frequency band of the sensors and the filtering cut-off frequencies all differ in the literatures, but the most common frequency range of the JAEs were between 50Hz and 500Hz. Mascaro et al. explored the frequency range from 50kHz to 200kHz with the notion that JAE techniques in structural monitoring usually explore the signals at a much higher frequency range (>20kHz) [20].

There is no consensus on which set of features produce the best results when classifying the JAEs into healthy or injured groups. Many features have been explored in previous studies [Shark][Frank][Befrui] and the three major subset of features are spatiotemporal, time-frequency, and statistical features. Additionally, a variety of classifiers have been tested such as neural networks, support vector machines, and logistic regression and provided accuracies ranging from 70% to 90%. Cai et al. used spatiotemporal features (form-factor, turn count with fixed threshold) and statistical features (variance of means) along with least-squares support vector machine and produced accuracy of 88.76% with area under the curve (AUC) of 0.95 [16]. Rangayyan et al. calculated spatiotemporal features (form factor) and statistical features (skewness, kurtosis, and entropy) and used neural networks with radial basis functions to obtain an AUC of 0.82 [15] Kim et al. used time-frequency features (mean and standard deviation of energy parameter, energy spread parameter, frequency parameter, and frequency spread parameter) and used back propagation neural network to get an accuracy of 95.4% [21].

2.3 Novel methods of processing JAE using *b*-value

2.3.1 b-value: a Potential Biomarker for Assessing Joint Health using JAE

The *b*-value represents a scaling of magnitude distribution of acoustical emissions. It is a measure of the relative number of large amplitudes to small amplitudes. In the field of seismology particularly pertaining to earthquakes, Gutenberg and Richter [22] proposed the empirical formula, expressed in Eq. (1), to quantify the logarithmic relationship between the magnitude and frequency of the shockwave generate by the shifting earth

$$\log_{10} N = a - bM_L \tag{1}$$

where M_L is the corresponding earthquake magnitude, N is the number of corresponding earthquakes larger than M_L, and a and b are the constants. The coefficient b which is the slope of the magnitude distribution represents the relative proportion of large to small fracture events occurred during the damage of the material. A high *b*-value is due to a large quantity of small acoustical emissions representing microscopic cracks. A low *b*-value indicates macroscopic, fast, and unstable crack growth accompanied by a high quantity of high amplitude acoustical emissions. To apply the Gutenberg-Richter formula to acoustical emissions, the magnitude term (M_L) is replaced by the amplitude of the acoustical emissions in decibels as follows in Eq. (2) and Eq. (3):

$$\log_{10} N_{AE} = a - bA_{dB} \tag{2}$$

$$A_{dB} = 20\log_{10}(V_{peak}/V_{ref}) \tag{3}$$

where A_{dB} represents the peak amplitude of the acoustical emission hit in decibels, and N_{AE} represents the number of acoustical emission hits with an amplitude greater than the predefined threshold. The *b*-value obtained in this relationship must be multiplied by a factor of 20 because the acoustical emission amplitude is measured in dB, whereas the Richter magnitude of an earthquake is defined in terms of the logarithm of its maximum

amplitude. Due to the variability of amplitude distributions and potential outliers, an 'improved *b*-value (*Ib*-value)' was proposed by Shiotani et al [23]. The *Ib*-value is defined as

$$Ib = \frac{logN(\mu-\alpha_1\sigma)-logN(\mu-\alpha_2\sigma)}{(\alpha_1+\alpha_2)\sigma} \quad (4)$$

where σ is the standard deviation of the detected clicks, μ is the mean amplitude of the detected clicks, α_1 and α_2 represent coefficients of upper and lower limits defined by the user. Previous studies have used this relationship for monitoring the progressive failure of various geologic materials (e.g. rocks, concrete, wood, fiberglass, etc) [24].

Our applications of this b-value statistic demonstrated a novel use of this analysis technique; specifically, the first ever application of b-value quantification in joint health assessment in both human subjects and human lower-limb cadaver model.

2.3.2 b-value Assessment on Pre- and Post- Recovery of Injured Subjects

2.3.2.1 Data Collection Protocol for Method Evaluation

All human subjects research was conducted under approval from the Georgia Institute of Technology Institutional Review Board (IRB) and for the DoD-funded portion of the work were also approved by the Army Human Research Protection Office. The dataset included knee JAEs from nine injured subjects and two measurements: the first measurement was taken within seven days of the injury, and the second measurement was taken four to six months following surgery and rehabilitation. The injuries included torn anterior cruciate ligaments, torn lateral menisci, and sprained medial collateral ligaments. At the time of the second recording, the subjects could resume regular functional activities.

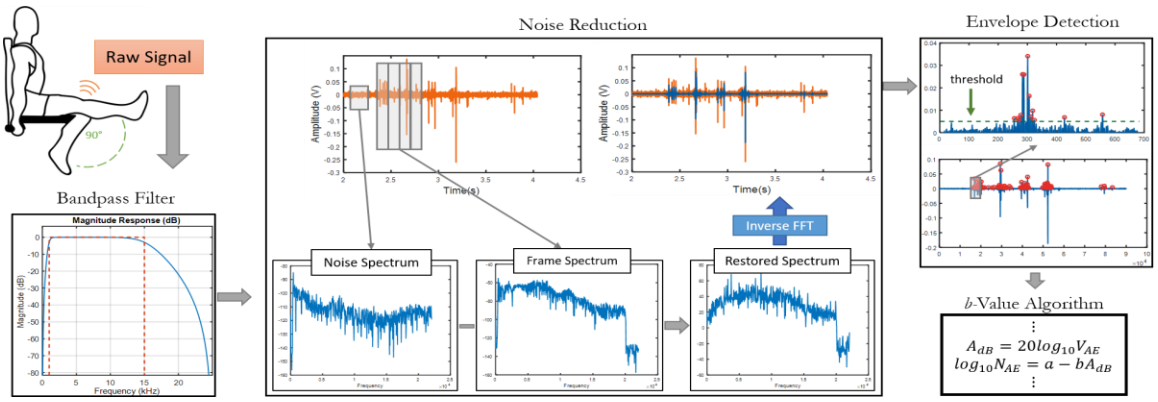

Figure 1 Click detection algorithm that consists of three steps: bandpass filter, noise reduction and envelope detection.

Fig. 1 provides an illustration of the measurement setup. For each subject, a low-noise, wide bandwidth electret microphone (COS-11D, Sanken Microphone Co., Japan) was attached to the medial and lateral aspect of the patella without directly contacting the skin. The COS-11D microphone was selected due to its small size, very low noise, high dynamic range, and fairly flat frequency response in the measurement range. The subject was asked to perform five unloaded knee flexion / extension exercises while seated without allowing the foot to contact the ground. The sounds measured by the electret microphones were recorded using an audio recorder (Zoom H6 Recorder, Zoom Corp., Japan) at a sampling rate of 44.1 kHz. Data collection was completed by Dr. Sinan Hersek and Dr. Caitlin Teague of Inan Research Laboratory and Michael L. Jones of the Exercise Physiology Laboratory at Georgia Institute of Technology.

In this work, we did not observe any distinct outliers of high or low amplitude in the acoustical emissions from the previously recorded joint sounds. Thus, we implemented a modified *b*-value analysis (Eq. 2 and 3). In recordings with distinct outliers in JAE amplitude, Equation (4) should be used instead. The changes in the *b*-value from the two measurements for each subject were compared to evaluate whether acoustical emissions

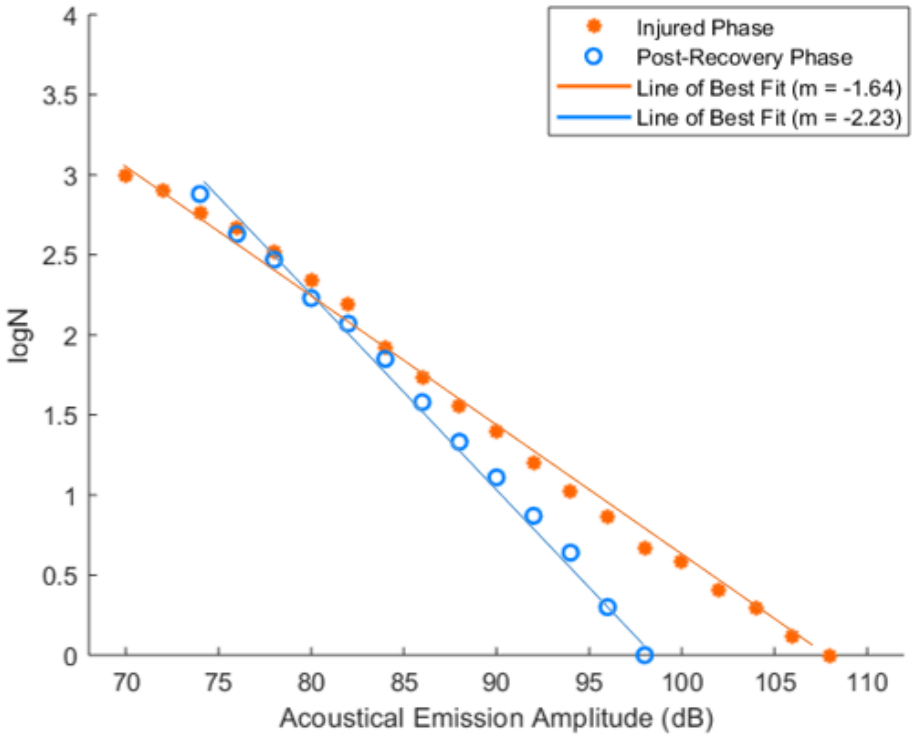

Figure 2. Cumulative occurrence frequency and the amplitude relationship plot of the acoustical emissions for injured and post-recovery phase for one subject.

from the knee joints could classify and quantify the knee's status as injured or healthy (i.e., recovered). The *b*-value is presented as the average of the *b*-values from each of the acoustical signals acquired from the microphones placed on the medial and lateral side of the patella.

2.3.2.2 Signal Processing

The principal goal of the signal processing was to detect high amplitude, short durations "clicks" in the acoustical signals—these are typically referred to as "acoustical emissions." First, the sounds acquired during five flexion / extension cycles from the knees of the subjects are digitally filtered using a finite impulse response band-pass filter with a bandwidth from 1kHz-15kHz. This bandpass filter removes the majority of the interface

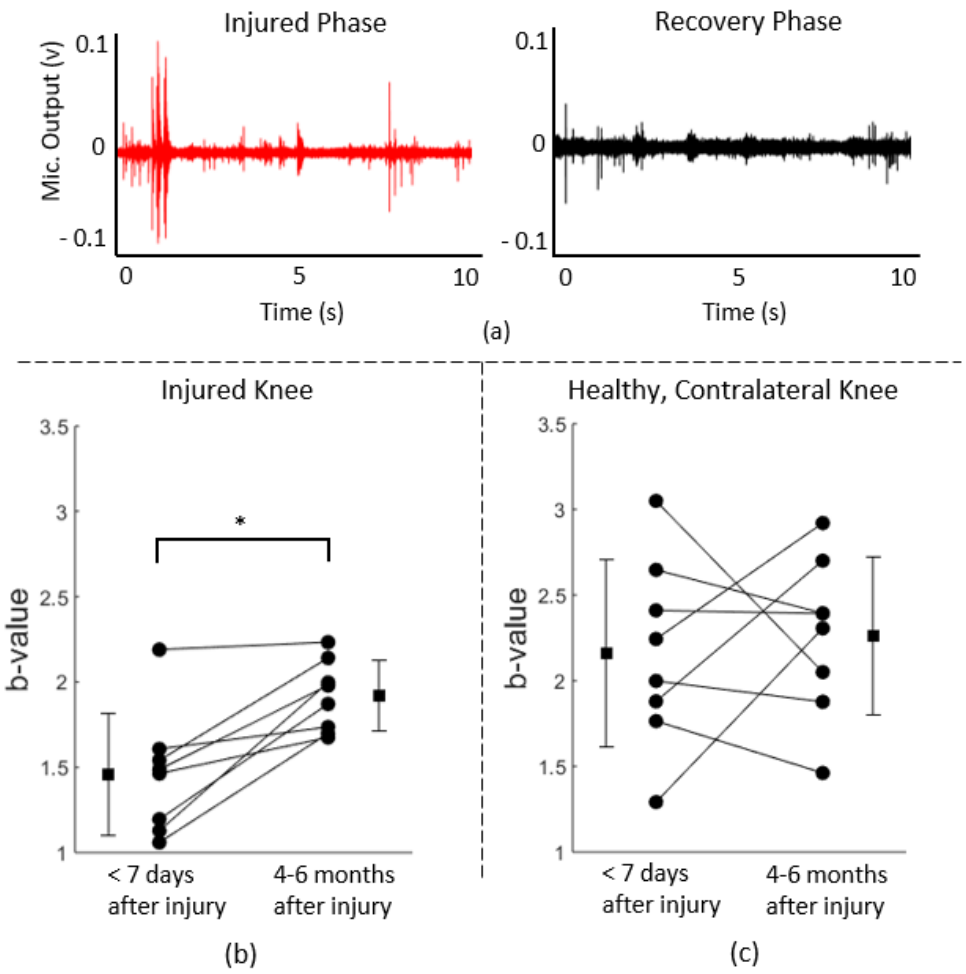

Figure 3 (a) An example 10 sec joint sound recording showing injured and recovered phases showing in the *b*-value for subjects (n=8) between the injured knee and the recovered knee (b) and showing no significant changes in the healthy, contralateral knee (c). There are more clicks with larger amplitudes in the injured phase than the recovered phase. The asterisk (*) represents significance ($p<0.01$).

noise in the signal, and prioritizes the bandwidth of the high energy, short duration joint sound signatures.

After this pre-processing step, we implement a spectral noise suppression technique to remove the static background noise [25] as illustrated in Fig. 1. The measurements had a static background noise recorded prior to performing the flexion / extension exercise and thus this segment was considered as the background noise model that we then removed

automatically. The sound data is windowed, and for each windowed segment we perform a fast Fourier transform (FFT) using a Hanning window and compute the expected value of the noise magnitude spectrum μN for each frequency bin. This is then subtracted from the signal magnitude spectrum and the differences having negatives values are set to zero. After the noise suppression, the signal is reconstructed using an inverse FFT. Then we use a modified envelope detection algorithm where the adaptive threshold is set as the sum of the root-mean squared and the maximum value of the reduced static background segment. This identifies the desired joint clicks from the acoustical emissions that are high-frequency and short durations. Once the clicks are detected, we calculate *N* which is the total number of clicks greater than the corresponding *AdB*. Using equation (2), we calculate the linear coefficients to obtain the *b*-value.

2.3.2.3 Results and Discussion

We calculated the *b*-values from two measurements: the first was at the time of the knee injury, and the second took place four to six months later. Fig. 2 shows the cumulative frequency-magnitude distribution plots of acoustical emissions corresponding to the injured and recovered phase for one subject to provide a means of visualizing how the b-value relates to peak amplitudes in the acoustical emissions waveform. A recording from one subject was found to be an outlier, likely attributed to a noisy measurement, and thus this subject was omitted for the analysis. Additionally, Fig. 3(a) illustrates an example of the difference between the injured and recovered phase.

For the entire dataset, the average *b*-value was 1.46 ± 0.35 for the injured phase and 1.92 ± 0.21 for the recovery phase. Fig. 3(b) provides a comparison plot of the *b*-values

calculated for all subjects. A paired sample t-test was performed to evaluate the statistical significance. This difference between the two groups (injured vs recovered) was statistically significant ($p<0.01$). There was an increase in the *b*-value of the acoustical emissions from the joints from the injured phase to the recovered phase in all eight subjects. We also calculated the *b*-values from the healthy, contralateral (i.e. control) knee to compare against the differences between the injured and recovery phase with the injured knee. The average *b*-value was 2.16 ± 0.51 for the injured phase and 2.26 ± 0.43 for the recovery phase. Fig. 3(c) provides all the *b*-values calculated for the healthy, contralateral knees of the same subjects. There was no statistical significance between the two groups suggesting that there is little to no change in the *b*-value in the contralateral (control) knee. Additionally, the values from the healthy knees were generally higher than the values from the injured knees. This indicates that *b*-value algorithm can be applied for one knee alone, and that it can be used as an absolute measure of knee health without the need for normalization. The results stated above indicate that the *b*-value can provide useful information about the knee sound patterns and enables one to discern between an injured knee and a recovered, healthy knee.

This section demonstrates that the *b*-value, extracted automatically from knee acoustical emissions, can quantify changes in the knee health for patients with acute injuries and throughout rehabilitation. This method of using the *b*-value greatly enhances the potential for incorporating a joint sound detection suite into a wearable system by allowing the device to be equally as effective in assessing knee health while requiring far less computational time and power. Future work will focus on optimizing the required number of cycles and quantifying whether the *b*-value follows the same pattern for multiple

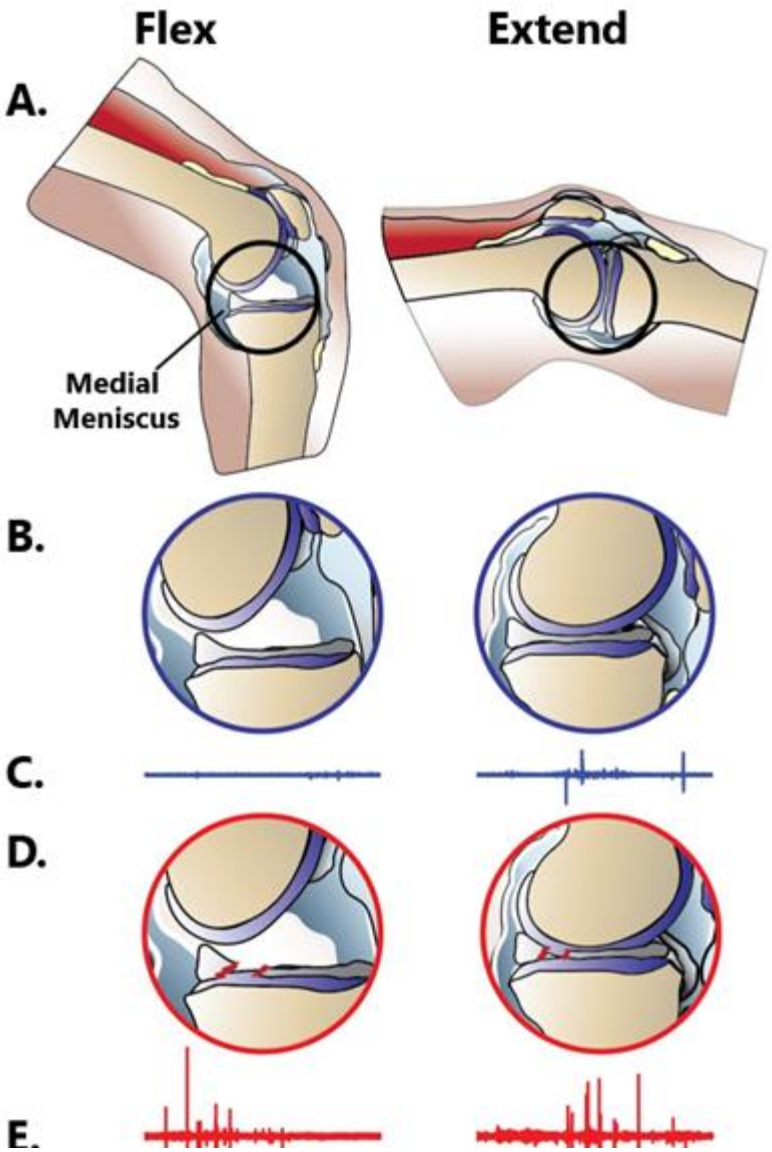

Figure 4. Concept model of knee acoustic wave creation before and after a meniscus tear with representative acoustic wave forms. A. Diagram of the knee during flexion and extension. B. Medial femoral condyle compressing the medial meniscus from flexion to extension. C. Representative acoustic waveform produced by the knee's movement. D. Compression of the radially torn, medial meniscus from flexion to extension. E. Representative acoustic waveform produced by the knee.

measurements over the course of rehabilitation. Additionally, the measurements required the use of expensive electret microphones. In future studies, we will investigate less expensive contact microphones for detecting joint acoustical emissions. Finally, the development of *b*-value measurement algorithms on a microcontroller would facilitate the

extraction of joint health in real-time with the system without the need for the full acoustical emission waveforms to be recorded or transmitted wireless. This could substantially reduce the power consumption and memory requirements for the system, and thereby enhance the potential for adoption by users for broad applicability in assisting the management of rehabilitation through sensor feedback.

2.3.3 b-value Assessment on Cadaver Lower-limb Model

In this work, we investigate JAEs using an injury model in human lower limb cadavers to better understand the nature of these JAEs. Previous studies to interpret acoustic emissions from the knee for clinical decisions has had limited success. One of the main reasons for this is a lack of mechanistic understanding of how these joint sounds are produced and what factors influence them. The cadaver model would allow a reproducible and more controlled analysis of the JAEs from the knee and understanding of the anatomical complexity and confounding physiological factors that occur in the specific structural change in the knee. The cadaver model was conceived by Dr. Geza Kogler, and the experimental design and implementation was conducted by Dr. Daniel Whittingslow of the Inan Research Laboratory. To better understand the source of these joint sounds and observe the changes in acoustic emissions from the knee, we created a medial meniscus injury model to better understand how alterations of the underlying anatomy can correlate with the JAEs recorded on the surface of the knee. Combining literature on internal joint pressure, our findings of minimum articulating surface distances, and joint sounds at each stage of injury led to our proposed model of joint sound production as shown in Fig. 4. To provide more physiologic context to the model, we next emulated the biomechanical alterations associated with swelling following an acute injury by serially injecting saline

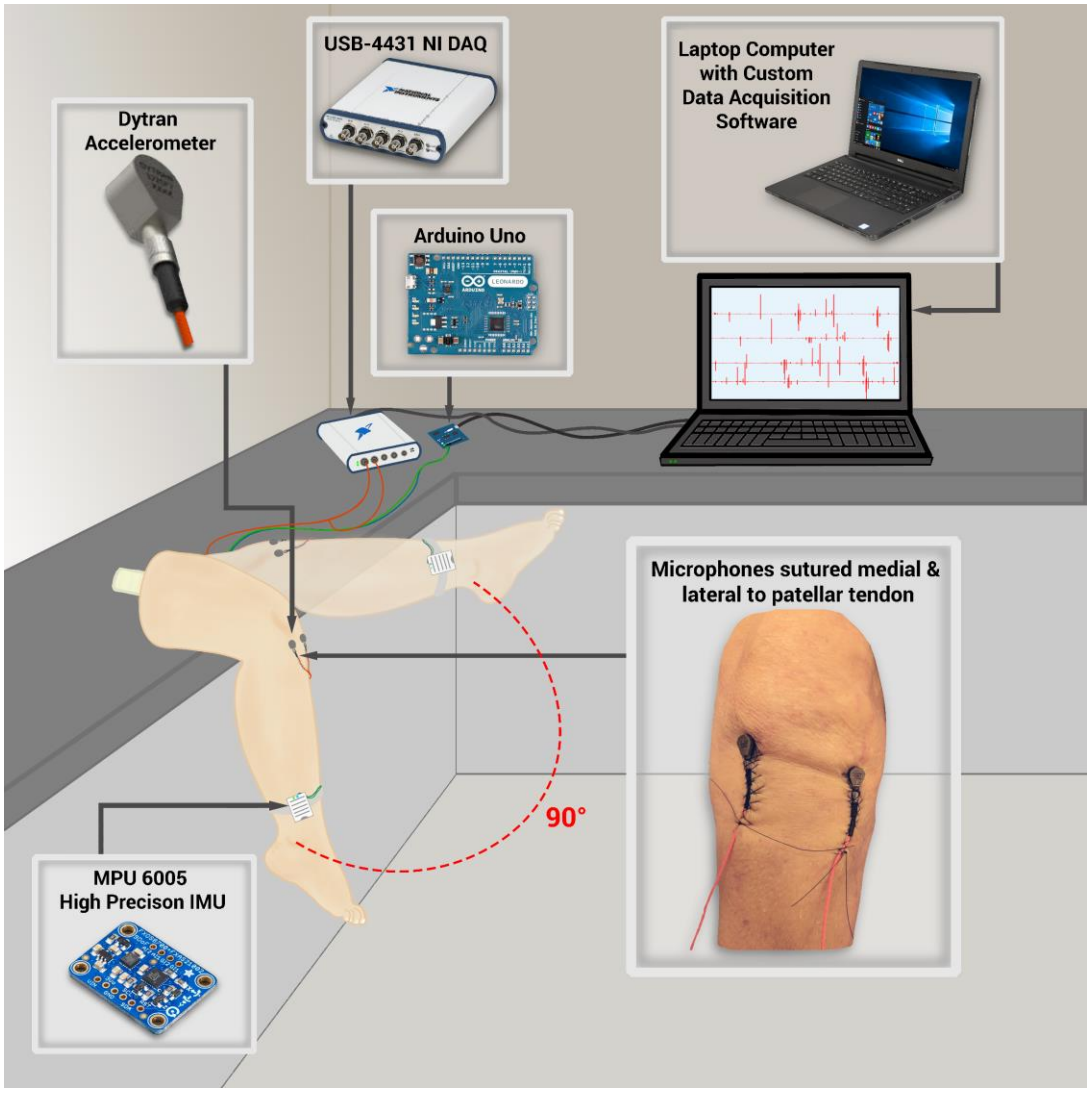

Figure 5 Testing setup for the generation, acquisition, and analysis of knee JAEs on a cadaver model. The cadaver knee is outfitted with two accelerometers and a high-precision IMU. The accelerometers are sutured medial and lateral to the patellar tendon and record the surface vibrations (JAEs) created by the manual flexion/extension of the leg. The IMU captures and syncs the 3D motion data to the joint sounds providing anatomical relevance to the recorded signals. A DAQ captures the audio waveform data and a microcontroller captures the IMU data. All data is transmitted to a laptop computer with custom acquisition and analysis software written in MATLAB.

into the joint capsule. The *b*-value of the acoustic emissions was calculated at each stage of testing. This sections represents the first time that an analysis of knee acoustic emissions has been performed on a controlled, cadaver model with incorporation of anatomical complexity, confounding physiological factors that occur in an injured state (i.e. swelling),

and specific structural changes in the knee. Our findings allowed us to propose a model of knee acoustic emission that better localized the source of these sounds while remaining consistent with the prior literature's findings that these sounds can be useful in classifying the health status of a knee [26, 27]. If characteristic alterations of these JAEs can be linked with knee health status, joint sounds may offer a biomarker for early detection and assessment of musculoskeletal injury.

2.3.3.1 Data Collection and Methodology

Nine fresh frozen human cadaver lower limbs were procured from MedCure, Inc (Orlangdo, FL, with permission for use in a research experiment) with an average age of 63.6 ± 9.5 years of age, stored at -20°C, and thawed to room temperature in a water bath for 8 h prior to testing. The age of these cadaver specimens may not be fully representative of the overall population, but the exclusion criteria helped limit the impact of confounding comorbidities. The joints were selected from donors with no known arthritis, injuries or past surgeries of the knee, and that were mobile at time of death. Prior to use, the legs were clamped to the laboratory benchtop and preconditioned with manual flexion/extension movements for five minutes. Two uniaxial analog accelerometers (3225F7, Dytran Instruments Inc. Chatsworth, CA) were sutured (4-0 Nylon Kit, Your Design Medical, Brooklyn, NY) 2 cm medial and lateral to the patellar tendon. These accelerometers have a broad bandwidth (2Hz-10kHz), high sensitivity (100 mV/g), low noise floor (700 μgrms), miniature size and low weight (1 gram). The medial and lateral patellar locations were selected due to the relatively unimpeded route (only a thin layer of muscle, tendon, and fat) to the articulating surface of the knee (where intra-joint friction is thought to produce the recorded vibrations [28].

To record the knee acoustic emissions, the cadaver legs were suspended on the side of a lab bench and passively flexed and extended through their full range of motion (~90° to 180°) every 4 seconds. This suspension ensured the cadaver limb did not contact the surface of the lab bench at any stage of the motion. The recordings contained a total of ten flexion/extension cycles with 5 seconds of background, environment noise recorded before and after. An inertial measurement unit (MPU6050, TDK InvenSense, San Jose, CA) was attached 5 cm proximal to the ankle and used to validate the joint angle and rotational velocity during these exercises. The signals from the accelerometer were sampled at 100 kHz and recorded using a data acquisition module (USB-4432, National Instruments Corporation, Austin, TX). The recording setup is illustrated in Fig. 5.

Each of the knees (n=9) were serially, surgically altered in four stages to isolate the effects that a medial meniscus tear has on the joint's acoustic emissions. The four stages of testing were baseline, sham surgery, meniscus tear, and the meniscectomy. After thawing and pre-conditioning, the joint sounds were first recorded at their baseline status. Next, a sham surgery was performed on the leg. The sham surgery was performed with the knee at 90° of flexion with a 5-cm oblique incision made just posterior to the superficial medial collateral ligament (MCL) at the level of the vastus medialis curving over the medial epicondyle onto the anteromedial aspect of the tibia. This cut exposed the interval between the posteromedial joint capsule, semimembranosus, and medial head of the gastrocnemius [29]. Next, the posteromedial joint capsule was cut 2 cm to expose the medial meniscus. Without damaging the meniscus, the incisions were closed with simple continuous, running sutures [30]. The sounds were recorded after this sham surgery status. Next, the meniscus tear was introduced by performing a 10mm transverse (radial) incision

on the posterior (zone A) portion of the meniscus. The surgical entry path was again sealed with a simple continuous running suture and the sounds were recorded. Finally, a meniscectomy was performed on the injured meniscus. The sutures were cut to re-expose the meniscus and a 5mm margin anterior and posterior to the transverse/radial meniscus cut was surgically removed. All the recordings took place after being sealed with a simple continuous running suture.

To emulate the altered mechanical environment within the knee resulting from swelling following acute injury [31], varying levels of saline were injected into the knees prior to meniscus surgery (n=5). 5 mL aliquots of saline were serially injected from 0 to 50 mL underneath the superolateral surface of the patella and directed posteriorly and inferomedially into the knee joint. After each injection, the joint sounds were recorded using the above acoustic emission acquisition protocol.

2.3.3.2 Signal Processing

The recorded signals were analyzed using MATLAB (MathWorks, Natick, MA). The signals were pre-processed using a digital finite impulse response (FIR) band-pass filter with 250Hz - 20kHz bandwidth to maintain emissions in the audible range while removing motion artifacts. Once filtered, the signals were synchronized to the (inertial measurement unit) IMU data and trimmed to remove the excess periods of noise before and after the flexion/extensions. This trimmed noise was then used as a basis for a noise suppression algorithm using spectral subtraction from the acoustic emission recordings [25]. The *b*-value metric was computed for the acoustic emissions to differentiate the sounds based on their amplitude distribution of the acoustic emissions. The mean and standard deviation

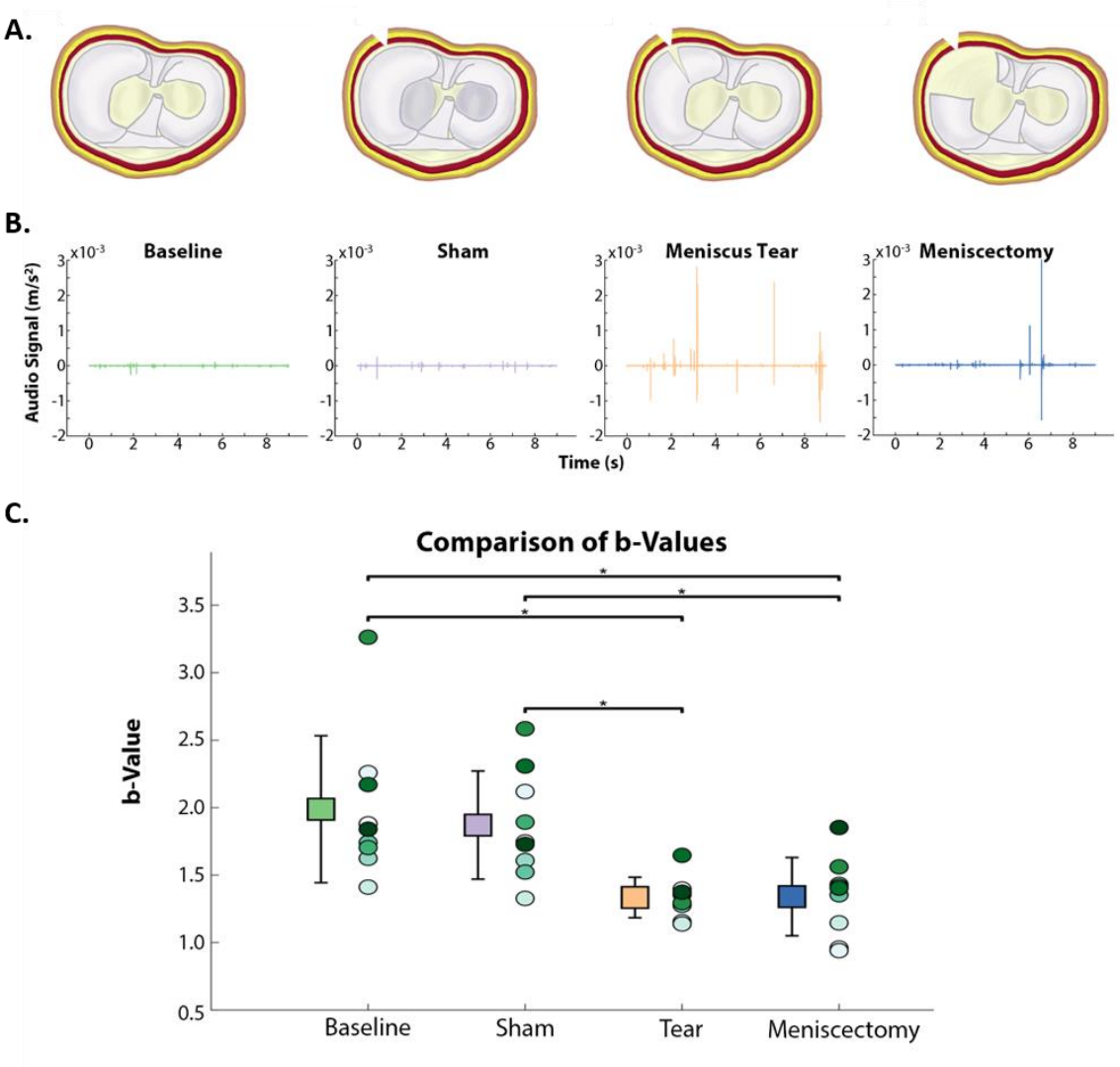

Figure 6. Acoustic data and *b*-values from four stages of meniscus intervention: baseline, sham, meniscus tear, and meniscectomy. A) Transverse plane view of tibial plateau diagram shown in order: baseline, sham surgery, posteromedial radial cut, and post-meniscectomy. B) Representative time-domain acoustical signal from one flexion and extension cycle at these four interventions. The meniscus tear signal has loud amplitudes compared to the baseline and sham and a slight decrease during meniscectomy. C) Boxplot showing the comparison of *b*-value across the interventions. There were statistically significant declines in the b-value from baseline to tear and meniscectomy, and from sham to tear and meniscectomy. (indicated with *, n=9 and $p<0.05$).

were calculated for each dataset. The data were assessed for normality using a Lilliefors test. It was found that the groups were non-normal, so the Scheirer-Ray-Hare extension of the Kruskal Wallis test was performed. This test is often used as a non-parametric

equivalent to the two-way analysis of variance (ANOVA) test. Finally, multiple Wilcoxon signed rank tests were performed to compare between the data groups. A Bonferroni correction was applied to correct for the multiple comparisons. The same series of tests were performed on the saline injection data.

2.3.3.3 Results and Discussion

The *b*-value statistic of the joint sounds at baseline was 1.99±0.54. After the sham surgery, the *b*-value dropped to 1.87±0.40. This shift was not statistically significant (p=0.25). This lack of statistical significance indicated that the sham surgery, with its alteration to the tissue external to the joint cavity and exposure of the joint capsule to the air and laboratory atmosphere, had minimal influence on the acoustic emissions of the knee. A full width, radial tear was performed on the posterior, medial meniscus. At this stage, the sounds appear much more chaotic, with several large spikes in the amplitude of the sounds. This increase in amplitude was reflected in the *b*-value after the meniscus tear (*b*-value = 1.33±0.15). This drop in the *b*-value was significant when compared to the baseline and sham stages (p=0.0039). This significance indicated that the meniscus tear was solely responsible for the change seen in the acoustic emissions. It indicates that knee acoustic emissions can differentiate the internal environment of the knee. After the meniscus cut was completed, the torn meniscus was removed resembling a meniscectomy. Qualitatively, the acoustic signal appeared to diminish at this stage from the meniscus tear state. When analyzed, there was a marginal increase in the *b*-value (1.34±0.29) toward the baseline/sham values. However, this increase was statistically insignificant when compared to the meniscus tear group (p=0.91). This lack of significant change in the *b*-value following meniscectomy indicates two possible outcomes: 1) The cadaver model was

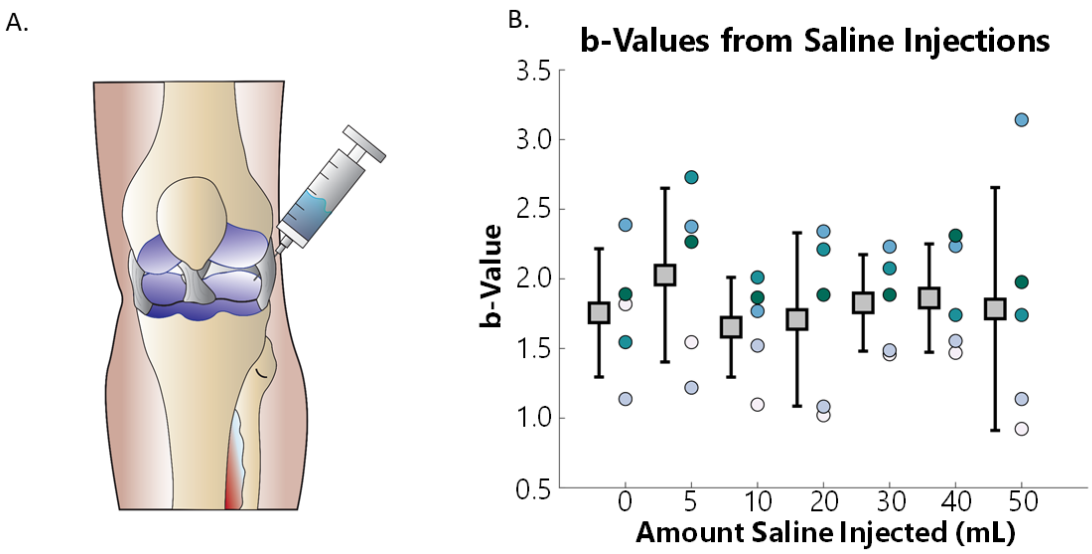

Figure 7 Acoustic Data and b-values from serial saline injections. Saline was serially injected from 0 to 50 mL into the joint cavity. (A) Demonstration of the superolateral approach used for injection of the saline. The corresponding b-values at each amount of injection are presented in (B). There were no significant differences from 0-50 mL of injected saline indicating that there was not a statistically significant change in the AEs of the knee from this intervention. (n=5, error bars= 1 standard deviation from mean of the b-value from the 5 legs tested.)

not a suitable substitute for a reparative treatment given the lack of blood flow/synovial fluid, or 2) this sensing modality may not be suitable for monitoring post-surgical repairs. In earlier work, the knee acoustic emissions were recorded from athletes at the start of their season and after suffering injuries such as torn anterior cruciate ligaments, torn menisci, and sprained medial collateral ligaments. In that study we found that the *b*-value and this sensing modality was able to track their recovery post-surgical intervention [27]. Thus, the lack of return toward baseline is most likely due to differences in the physiology/anatomy of the cadaver model and young, collegiate athletes.

After a meniscus tear occurs *in vivo*, a series of physiologic events begin in response to the injury. Principal among these regarding the effect on mechanical articulation is

localized swelling. To better understand the extent to which this swelling affects joint acoustic emissions we serially injected 5 mL aliquots of 0.9% saline solution into the knee capsule (Fig. 7 (A)). After each injection, the acoustic emissions were recorded, and *b*-values were calculated. The *b*-values ranged from a minimum of 1.6±0.3 to 2.1±.6. The data were highly variable with no clear trends or statistical significance ($p>.05$ for $n=5$) (Fig. 7 (B)). Therefore, the injection of saline into the knee capsule does not directly influence the production or propagation of acoustic emissions.

The section presents the first time that knee acoustic emissions have been characterized in a controlled setting with a cadaver model of knee injury. The insights gained on the application of acoustic emissions for identifying meniscus tears are promising and warrant future work in the field. The relation between joint anatomy, the associated interactions upon articulation, and the resulting acoustic emissions should be further explored to help understand the full utility of this novel sensing modality. With more research, joint acoustic emissions could soon serve as a readily measurable, non-invasive biomarker of joint health.

CHAPTER 3. QUANTIFYING THE EFFECTS OF INCREASING MECHANICAL STRESS ON KNEE ACOUSTICAL EMISSIONS

3.1 Introduction

This chapter seeks to expand the scope of JAE assessment beyond chronic conditions and acute knee injury and instead focus on quantification of knee joint loads. One aspect that is of interest clinically and scientifically is the quantification of vertical loading forces experienced by the knee throughout daily living activities and exercises. Prior work in estimating knee loading forces has used instrumented knee implants to quantify loading *in vivo* [32], or biomechanical modeling techniques to estimate loading profiles [10]. However, estimation of vertical loading forces in the knee using wearable, non-invasive sensing has never been previously demonstrated. In this work, we investigate whether the characteristics of acoustical emissions from the joint change in a quantifiable and monotonic manner in response to increased biomechanical stress on the joint during a standard movement. We predict that as the internal stress on the knee increases, additional interactions between the articulating surfaces may occur and cause a more complex acoustic profile. Fig. 8 provides an illustration of our hypothesis and shows the measurement setup used for assessing loading effects, based on a vertical leg press with varying weight and the measurement of acoustical emissions from the knee. We leveraged graph mining algorithms [33] to quantify this complexity and evaluated our approach in a study of able-bodied subjects.

Figure 8. Illustration of the effects of vertical loading forces on the acoustic emissions resulting from increased biomechanical stress on the internal surfaces in the knee

Table 1. Demographic Data for Study Participants

	Male	Female
Number of Subjects	9	3
Age (mean ± σ, in years)	24.3 ± 1.9	25.3 ± 2.1
Height (mean ± σ, in cm)	175.1 ± 3.5	155 ± 2.7
Weight (mean ± σ, in kg)	74.3 ± 9.9	50.7 ± 7.2

3.2 Data Collection and Methodology

Twelve healthy subjects with no prior injuries were recruited for the study which was approved by the Georgia Institute of Technology Institutional Review Board (IRB). For each subject, four miniature contact microphones (BU-23173-000, Knowles Electronics LLC., USA) were attached to the medial and lateral sides of the patella and superficial to the lateral and medial meniscus using Kinesio Tex tape (see Fig. 8(a)). The anatomic

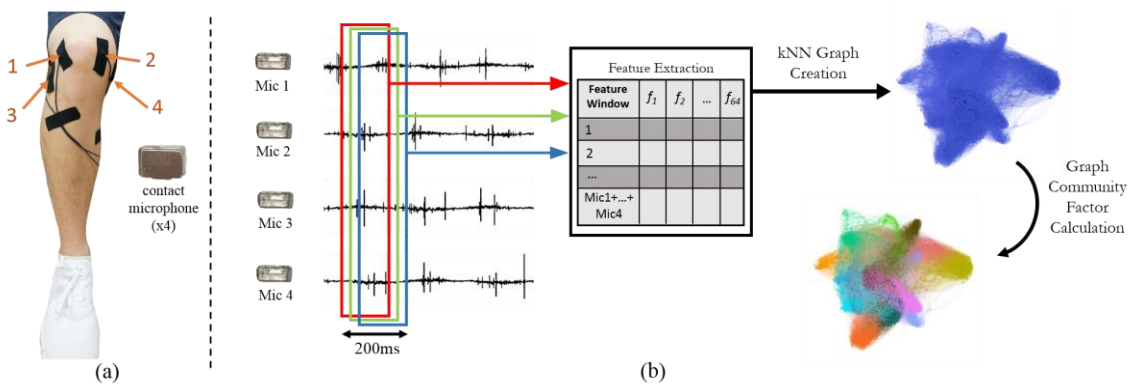

Figure 9. Sensor placement and overview of the method of how the signals acquired are analyzed. (a) Four contact microphones are placed on the medial and lateral sides of the patella and superficially to the medial and lateral meniscus (b) The signal analysis workflow for knee joint sounds. The signals from the dominant knee of the subjects are filtered and standardized (to zero mean and unity variance) and windowed (frame length of 200ms with 90% overlap). The features are extracted for all four mics and vertically concatenated where columns represent the features and rows represent all the windowed segments. The rows represent all the windows in microphone 1 to microphone 4 and the columns represent the 64 features. A k-Nearest Neighbor graph (kNN graph) is constructed from the matrix formed using data from the dominant knee and calculates the graph community factor (GCF) using the graph community detection algorithm.

positions were selected because of their ease of use as prominent landmarks for repeated placement of the microphones between subjects. The biomechanics of the joint was also considered in choosing these placement locations. The patella experiences significant frictional forces from the movement of the quadriceps tendon during flexion extension and is directly superior to the articulating surfaces of the femur and tibia. The menisci are a pair of crescent-shaped, fibrocartilaginous pads that provide structural integrity to the knee when it undergoes torsion and tension and can disperse the load and relieve friction over the articular surfaces of the femur and tibia in the knee. As we increase the compressive forces to these locations with external loading, we expect to see a change in the emitted sounds by the complex interaction between these surfaces. The contact microphone, which are piezoelectric sensors with broad bandwidth (>20kHz) and low output noise (7 µVrms

"A" weighted), were selected as they provide high quality acoustical pick-up from the body while maintaining a small footprint amenable for wearable use. The subjects were then asked to perform ten repetitions of vertical leg press with different loading conditions. Vertical leg press was selected as the exercise for this study since it allows for vertical loading at the knee joint to be varied in a controlled manner up to a sufficiently large load (i.e. body weight) to notice effects on the acoustical emissions. There was a total of four loading conditions, starting with zero load (no weights), and increasing by a third of the subject's body weight up to the full weight of the subject. The audio signals from each microphone were pre-amplified using a custom analog front-end consisting of a voltage regulator, setting a 3V supply used for powering the microphones and amplifiers, a low noise amplifier with a voltage gain of 100, and 180kHz bandwidth, and a bandpass filter (bandwidth: 16Hz-20kHz, Butterworth). The amplified signals were then sampled at 50kHz (16bits/sample) using NI USB-6225 data acquisition hardware (NI, Austin, TX, USA). All signals were recorded on a laptop using LabVIEW System Design Software (NI, Austin, TX, USA) and were processed using MATLAB (The Mathworks, Naticks, MA, USA) and RStudio (RStudio, Boston, MA, USA).

Table 2. Audio Features for Knee Joint Sounds

Feature Name	Equation	General Description and Significance
Energy	$E(i) = \sum_{n=1}^{W_L} \lvert x_i(n)\rvert^2$	Total signal energy Short term energy is expected to exhibit high variation over successive speech frame
Zero Crossing Rate	$Z(i) = \frac{1}{2W_L}\sum_{n=1}^{W_L} \lvert sgn[x_i(n)] - sgn[x_i(n-1)]\rvert$	Rate of sign changes: - Exhibit higher values in the case of noisy signals (i.e. noisier if there is higher loading forced on the knee joints)
Energy Entropy	$H(i) = -\sum_{j=1}^{K} e_j \log_2(e_j), \quad e_j = \frac{E_{subFramej}}{E_{shortFramej}}$	Measure of abrupt changes in the energy level: - Low value in abrupt energy changes (i.e. low peaks if there are higher loads affecting the joints)
Spectral Centroid and Spread	$C_i = \frac{\sum_{k=1}^{Wf_L} kX_i(k)}{\sum_{k=1}^{Wf_L} X_i(k)}, \quad S_i = \sqrt{\frac{\sum_{k=1}^{Wf_L}(k-C_i)^2 X_i(k)}{\sum_{k=1}^{Wf_L} X_i(k)}}$	Center of gravity of spectrum/ second central moment of spectrum: - Higher values correspond to brighter sounds (i.e. brighter sounds if higher loads are endured on the joints)
Spectral Entropy	$\mathrm{H} = -\sum_{f=0}^{L-1} n_f \log_2(n_f), \quad n_f = \frac{E_f}{\sum_{f=0}^{L-1} E_f}$	Like entropy but in frequency domain: - Higher value in sounds for more loads on the joints
Spectral Flux	$Fl_{i,i-1} = \sum_{k=1}^{Wf_L} \left(EN_i(k) - EN_{i-1}(k)\right)^2$	Measure of spectral change between two successive frames: - Lower value if the signals are more consistent (i.e. lower the values will be as more loads affect the joint sounds)
Spectral Rolloff	$\sum_{k=1}^{m} X_i(k) = C\sum_{k=1}^{Wf_L} X_i(k)$	Frequency below which 90% of the signal energy (magnitude) is concentrated: - Higher value for wider spectrum (i.e. higher in joint sounds with more loads are enforced)
MFCCs	$c_m = \sum_{k=1}^{L} (log\widetilde{O_k}) \cos\left[m\left(k-\frac{1}{2}\right)\frac{\pi}{L}\right], \quad m = 1, 2, \ldots, L$	Coefficients that make up a representation of the short-term power spectrum of a sound, based on a linear cosine transform of a log power spectrum on a nonlinear mel scale of frequency: - First 13 MFCCs carry enough discriminative information to compare joint sounds with different loading conditions
Band Powers	$\mathrm{BP_i} = 2\int_{f_1}^{f_3} \lim_{T\to\infty} E\left[\left\lvert\frac{1}{\sqrt{T}}\int_0^T x(t)e^{-i2\pi ft}dt\right\rvert^2\right]$	Power of the signal in 29 distinct frequency bands, between 30 logarithmically spaced frequencies in the range of 1kHz-15kHz: - Higher frequency band powers will exhibit high values at frames where joint sounds are most abrupt. (i.e. joints affected by more loads will have higher values)

3.2.1 Signal Pre-processing and Feature Extraction

The acoustical signals were acquired during ten repetitions of vertical leg press cycles on the dominant leg of the subject. The signals were digitally filtered using a Kaiser-window finite impulse response bandpass filter with a bandwidth of 400Hz – 20kHz to remove the low-frequency interface noise between the tape, the skin and the microphone. The filtered signals were standardized with zero mean and unity variance to balance out any variations in the signal amplitude among sensors that could result from differences in contact pressure against the skin. The normalized signals were then divided into segments (windows) with a duration of 200ms and 90% overlap between successive segments. This segment duration and the overlap allowed multiple joint sound signatures to be present within a given frame. The features derived from each segment are summarized in Table 2 and many of them are described in detail in Giannakopoulos, et al. [34]. The features were selected empirically and are commonly used in other audio signal processing applications. For example, the mel-frequency cepstrum coefficient (MFCC) [35] is prevalent in speech recognition analysis, for discriminating speech, music, and background noise [36].

For each windowed segment of each microphone, a total of 64 features were extracted and stored in a vector. For each loading condition, we vertically concatenated the features extracted from the windowed segments of all four microphones into one single matrix.

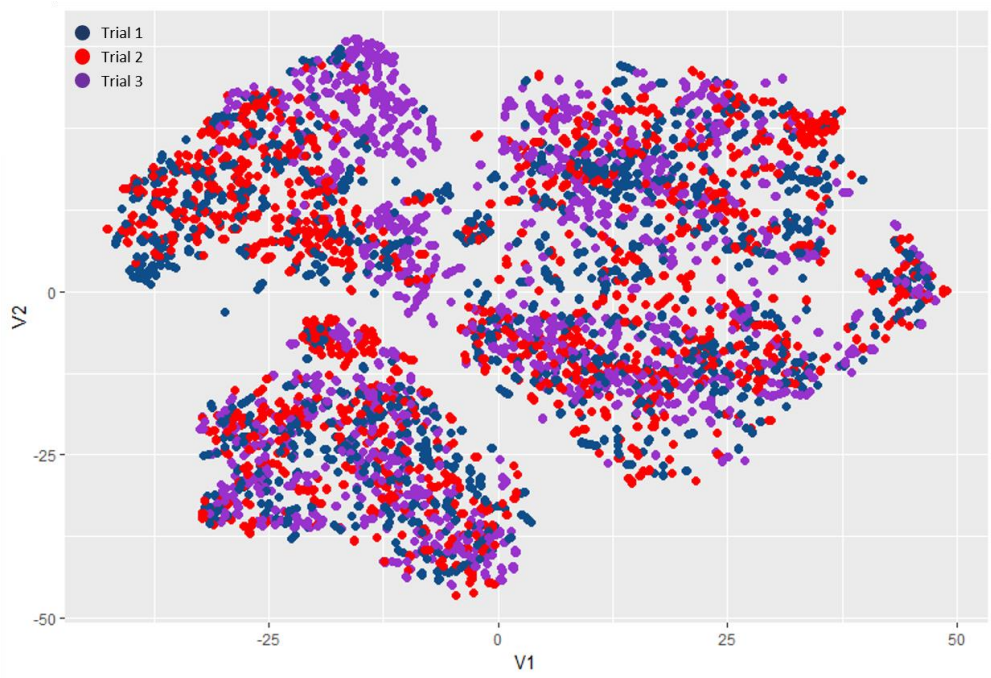

Figure 10. A visual representation of the audio signal frames for three different trials on one subject for one of the loading conditions (two loads) using t-Stochastic Neighbor Embedding (t-SNE). The clusters from the three different trials heavily overlap indicating that the measurements are repeatable.

Based on the common statistical learning rules found in [38] and [39] the number of features acquired for our dataset is a reasonable value.

3.2.2 Repeatability Testing

To test the repeatability of the measurements of placing the sensors and loading the joint, we have analyzed the acoustical emissions from five subjects over three different trials from different days using t-Stochastic Neighbor Embedding (t-SNE). This technique, t-SNE, reduces dimensionality by constructing a probability distribution over the points in the high-dimensional feature space and a similar probability distribution over the points in the low-dimensional map while minimizing Kullback-Leibler divergence between the two distributions with respect to the locations of the points in the feature space [40]. This

minimization ensures that the mappings maintain the relations between each data point in the high dimensional space in the newly calculated low dimensional space. Each data point represents a 200ms frame of the acoustical signals acquired while the subject performed one leg press. For visual representation, 64 feature set (64 dimensions) is reduced to two dimensions as shown in Fig. 10. Note the labels on the axis do not have any physical meaning, and instead describe the two calculated axes from the t-SNE dimension reduction. For each loading conditions, the plot showed little to no separation within the clusters of data points for three different trials. This indicates that the signals can be consistently measured from one day to the next.

3.2.3 Proof-of-Concept Study of Loading Effects during Walking

We considered an alternative exercise using an AlterG (AlterG, Inc., Fremont CA., USA), an anti-gravity treadmill that assists rehabilitation of patients by off-loading body mass during weight-bearing exercise [41]. Testing was performed on the AlterG treadmill because of its ability to alter the body weight (or load) on the knee joints while walking. This exercise provides a more real-world context to the nature of joint acoustical emissions during an everyday activity. The AlterG assessments further tested our proposed concept that an increased load on the joint leads to an increasingly complex acoustical emission. llustrations for the measurement setup and the exercise movement are depicted in Fig. 15(a) and 15(b). The microphone placements were the same as the locations for the vertical leg press. In the case of the AlterG device, we were able to decrease the load on the joint and thus test our hypothesis on joint loading conditions that were less than body weight during walking. Given that this exercise, and thus the movement/loads of the joint, are different

between walking and performing leg presses, no cross comparisons across exercise are performed.

As a proof-of-concept, we recruited three subjects, under an IRB approved protocol, to perform 20 seconds of walking on the treadmill with two different weight conditions: 20% of the body weight (minimum), and 100% of the body weight (maximum). The walking speed was kept constant at a speed of 2.0mph. While the sounds were recorded during the entire gait phase, the preprocessing of the signals during gait required different approach as the sounds recorded during the heel strike could only depict the noise caused by the foot hitting the ground which obscures any knee joint sounds we hoped to record. As such, this period of heel strike (the first 5% of gait cycle) was omitted from the analysis and the rest of the stance phase (5% to 50% of gait cycle) and swing phase (50% to 100% of gait cycle) were used in this analysis.An inertial measurement unit was synchronously recorded to define the stance and swing phase of the gait cycle. After this preprocessing step, the signal processing and feature extraction methods were used to derive a qualitative metric.

3.3 Graph Mining Algorithm

Our hypothesis is that increasing the vertical loading forces on the knee would increase heterogeneity among acoustical signals captured by the microphones. To investigate this matter, we utilized the concept in graph theory of quantifying heterogeneity by locating, and computing the number of, communities within the graph. We considered the combined features from microphones for a single loading condition as a data matrix X**.** Accordingly, the distribution of X should be modeled. Although this can be done using

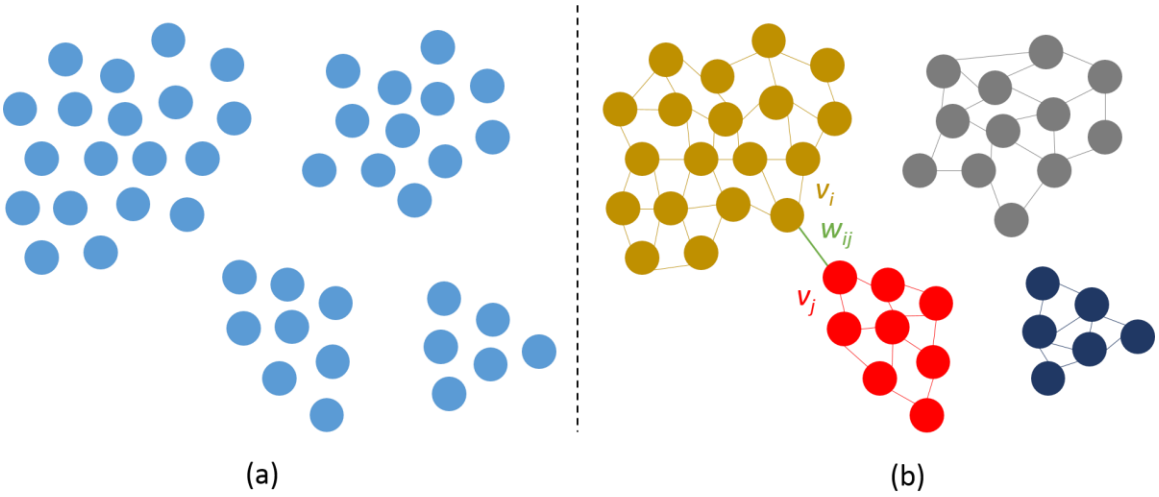

Figure 11. An example illustration of the clustering of the node (degree of 4). (a) General depiction of the dataset (b) Example graph where v_i and v_j represents vertex in the nodes and w_{ij} represents the weight of an edge between the two nodes.

some statistical models such as Gaussian or student t-distributions [42], these techniques require strong assumptions about the high-dimensional shape of the data (e.g., ellipsoid versus convex) and model parameters (e.g. mean and standard deviation) which can cause many problems, such as unreliable bandwidth estimation for applied kernel density function.

To overcome these challenges, we reconstructed a k-Nearest Neighbor graph (*kNN*) from graph theory which previously has been successfully used by researchers to model and cluster high dimensional bioinformatics data [43, 44]. Our idea is that the constructed graph from a knee which experienced smaller loads should be less heterogeneous than the one that experiences higher loads. This heterogeneity can be modeled with the number of complex communities in the related graph: a greater number of graph "communities" should be needed to describe sounds emitted from a knee which is loaded with higher forces.

In this work, we define a *kNN* graph for each dataset *X*. Let *KG = {V, E}* indicate the

kNN graph corresponding to X where $V = \{v_1, v_2, \ldots, v_N\}$ is the set of vertices and $E \subseteq V \times V$ represents the set of edges among v_i. In this graph, each vertex v_i indicates one row (acoustical window) in X. To model the local neighbor of each window x_i in X, the corresponding vertex v_i is connected to its k nearest neighbors using Euclidean distance. Fig. 11 illustrates how each windowed segment will be grouped and differentiated into separate clusters. In this work, k was chosen to be 10 empirically. Other values were also investigated (e.g. 5-15) and similar results were obtained.

If we only consider the Euclidean distance values [45] to assign related weights of edges between v_i with its nearest neighbors, noisy data points would engender many problems. If there are some v_is expanding the dispersed zones between two different communities, we may not distinguish these two communities and merge them as one single community incorrectly. Hence, weights are reassigned to each graph edge using dice similarity [46], such that we incorporate the properties of each point's neighborhood rather than relying on Euclidean distance alone in attributing points to clusters or communities. The dice similarity of v_i and v_j means twice the number of common neighbors divided by the sum of the degrees of v_i and v_j. Assuming v_i and v_j indicate two connected vertices within the kNN graph, the assigned weight for the edge between these two vertices is defined as,

$$w_{ij} = \frac{2*|\{A_i \cap B_j\}|}{(|D_i| + |D_j|)}$$

where A_i and B_j denotes the set of the neighbors of v_i and v_j, respectively. Also, the degree of v_i and v_j are represented as D_i and D_j, respectively and finally, the notation |*| is the number of elements in a set. Fig. 3.4(b) shows how the calculated weight will allow two edges, v_i and v_j, from different clusters not to be merged. Once the weighted *kNN* graph is

extracted, a community detection algorithm is applied to extract all the potential communities (clusters) within the *kNN* graph [47]. In this work, the Infomap community detection algorithm [48] is employed to quantify the communities of the *kNN* graph, since Infomap has been applied successfully in various areas of graph mining in different fields such as bioinformatics [49]. Infomap uses the probability flow of random walks on the network as a proxy for information flows and clusters the graph into multiple communities [50]. The algorithm searches for a partitioning of the *kNN* graph to minimize the expected description length of a random walk and seeks to compress

the description of information flow visited by a random walker on the network. Using Huffman code [51], all v_i visited by a walker are recorded and coded. The walker takes a reasonable amount of time within the same community which results in longer walking process. The computational complexity of this algorithm is approximately O(|E|). The number of detected communities is shown with "GCF" (Graph Community Factor) which represents the heterogeneity of extracted *kNN* graph from the data matrix *X*.

One important note is that discovering of the potential communities in the *kNN* graph is tantamount to finding the number of clusters (dense areas) in a high dimensional dataset X. Applying regular clustering methodologies such as K-means and Gaussian Mixture Models are not possible in this problem, as these methods require the knowledge of the number of clusters (dense populations of acoustical windows) within the data matrix. We also note that applying a kernel-based density clustering algorithm [52] (as it automatically estimates the number of dense areas in data) on a 64-dimensional dataset X to find the clusters is challenging and not practical. The difficulty is that the curse of dimensionality causes the density detection in high dimension (in this problem 64) to be very time

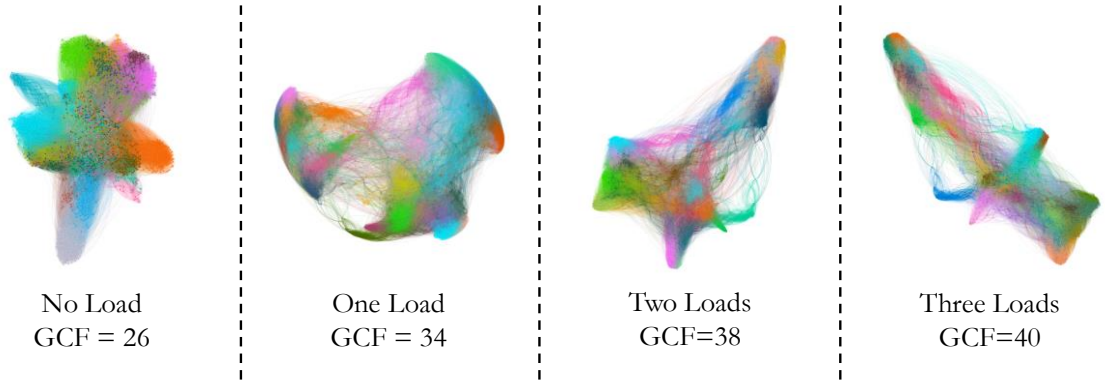

Figure 12. Graphs created based on the sound features for all windows of the recording and calculating the GCF score. Example graph from one subject is shown with the associated loading condition and GCF. Different colors correspond to different groups of clusters, implying that higher GCF value represents more variation of colors in the graph.

consuming and statistically not robust.

3.4 Results and Discussion

3.4.1 Changes in the GCF with Loadings for All Microphones

We evaluated the use of the graph mining algorithm to quantify the changes of acoustical emissions from the knee joints with respect to different vertical loading forces on twelve subjects. Four contact microphones were used to collect the joint sounds from various locations on the knee (medial and lateral of patella and meniscus). Fig. 12 illustrates the increasing trend of heterogeneity and the calculated GCF value with respect to different loading conditions for one representative subject. The knee graph is constructed from the individual loading data matrix where each data point (vertex in the graph) represents all the time and frequency domain features for one windowed frame of the acoustical emissions and different colors characterize different communities. The graph on the far left of Fig.12 represents densely clustered nodes that are more homogeneous and closer to one another in high dimensional space. As the loading conditions increase, the set

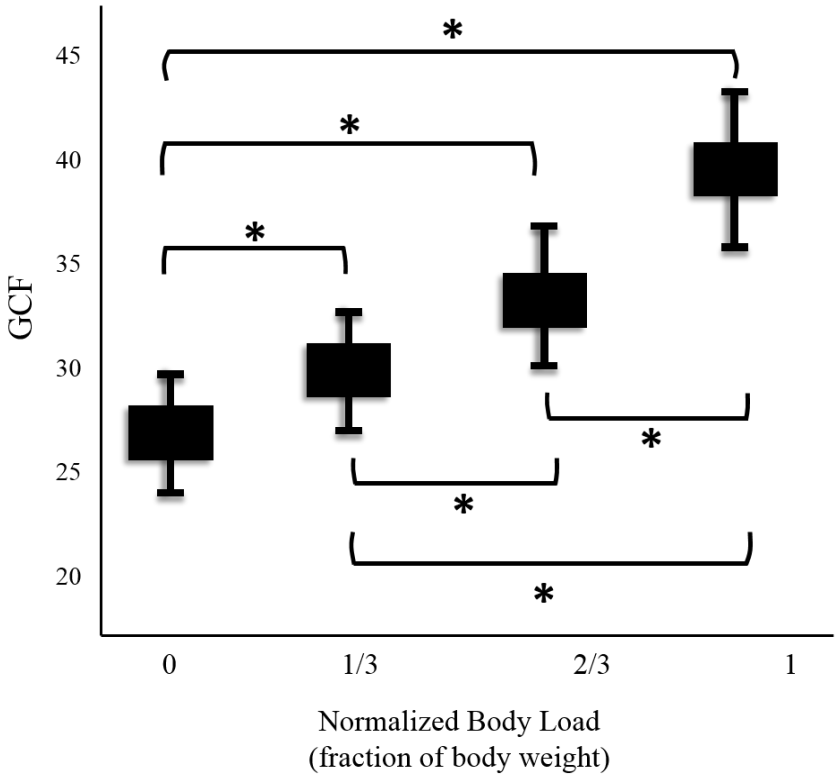

Figure 13. Boxplot showing GCF increases with loading for subject (n=12), indicating more heterogeneity for all acoustical signatures. The asterisk (*) represents the p-value less than 0.01 which is calculated using a non-parametric paired Kolmogorov-Smirnov test.

of nodes in the graph become heterogeneous and geometrically more dispersed in space indicating a more variable feature set. The mean GCF values for no loading, one-third body weight (BW), two-thirds BW, and BW were 26, 34, 38, 40, respectively. Fig. 13 provides a boxplot of the GCF values calculated for all subjects for each loading condition. The mean values for no load, one-third BW, two-thirds BW, and BW were 30, 32, 36, and 39. Since the sample size is not large, the non-parametric paired Kolmogorov-Smirnov test was used to calculate the p-value ($p<0.01$). For twelve subjects, we demonstrated the increase in GCF of the acoustic emissions from the joints with respect to the increasing load level on the knee.

3.4.2 Changes in GCF Across Microphones

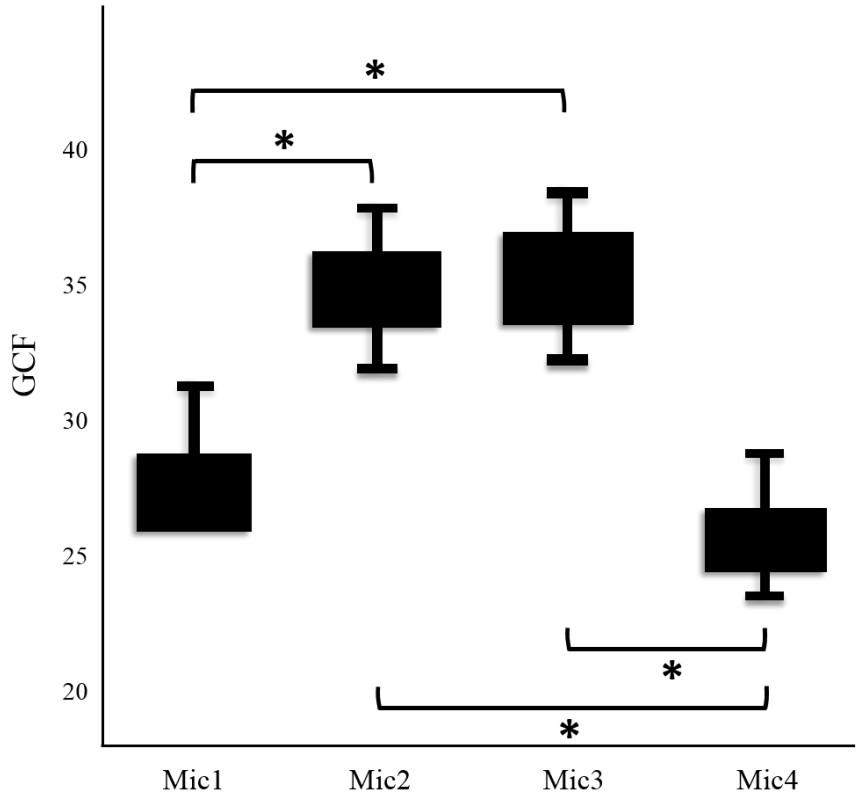

Figure 14. Boxplot showing GCF for different microphones (locations on the knee). The data matrix consists of all loading conditions per microphone for each subject. The asterisk (*) indicates the p-value less than 0.01 which is calculated using a non-parametric paired Kolmogorov-Smirnov test.

We also evaluated the characteristics of the acoustical signals across four different microphone locations to determine which locations had the most heterogeneity. Each microphone data matrix consists of all the segments and the features for the four loading conditions. Fig. 14 shows the boxplot of average GCF value for all subjects with respect to the microphone locations (numbers). Microphones 1,2,3, and 4 have mean GCF values of 26.4, 32.6, 33.5, and 23.8 respectively. We used the same non-parametric paired Kolmogorov-Smirnov test to calculate the p-value ($p<0.01$). Referring to Fig. 9(a), the results showed that locations 2 and 3 (medial side of the patella and superficial to the lateral

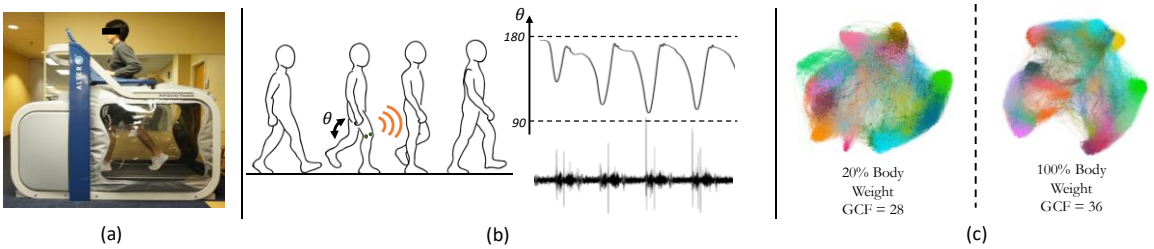

Figure 15. Alternative exercise that can measure joint sounds with different loads. (a) AlterG device allows the user to reduce their body weight by a designated percentage down to 20 percent. (b) Illustration of the activity and measurements of acoustical emissions from the joint with contact microphones with respect to the angle of the dominant knee. (c) Graphs created based on the sound features for all windows of the recording and calculating the GCF score. Example graph from one subject is shown with different percentage of the body weight.

meniscus, respectively) seem to show higher variation than the microphones placed on 1 and 4 (lateral side of the patella and superficial to the medial meniscus, respectively). The underlying anatomical sources of this variation are hypothesized as follows: microphone 1 is located on the superior lateral aspect of the knee which is principally superficial to the femur, quadriceps tendons, muscle, and fat. Microphone 3 placement includes the tibia collateral ligament, muscles, and the semi-membranous bursae, a jelly filled sacs in between ligament and bone, along with the previously mentioned lateral meniscus and associated connective tissue. In addition, the fibula connects to the tibia on this side of the leg, which could cause considerable differences from the sounds produced on the opposite side. The fibular collateral ligaments are located on the lateral side, close to microphone 3, which could contribute to more heterogeneity in that location since it is another source of tension on the joint when load is applied. Locations 1 to 4 (lower heterogeneity) and locations 2 to 3 (higher heterogeneity) makes an ‘X’ through the knee. There are several anatomical structures that follow a similar course through the region, and as such may be particularly potent contributors to the variations and heterogeneity seen. These structures

include the two proximal heads of the gastrocnemius, the popliteus muscle/ligaments, and the anterior cruciate ligament (ACL) and posterior cruciate ligament (PCL).

3.4.3 Changes in GCF during Walking with Loading

From the walking dataset, using the graph mining technique from the acoustical signal obtained from three subjects, we found that the average GCF value increased from 26 to 33 as the body weight changed from 20% (minimum) to 100% (maximum), respectively (see Fig. 15(c)). This showed that changing the loading on the knee while walking has an impact on the knee joint acoustical emissions.

3.5 Conclusion

This work established a method of using a graph mining algorithm to quantify the impact that mechanical loading of the knee has on the joint sounds produced. We demonstrated that with increasing loading conditions in both leg press and walking, the acoustical emissions became more heterogeneous. Furthermore, we observed that there were more variations in microphone placement at the medial side of the patella and the lateral side of the meniscus.

Future work will include investigating the causes for the variation in signals due to microphone placement and which locations would provide the best signal quality. This will include a cadaveric dissection with microphones placed on the aforementioned anatomical structures. On the skin, microphones will continue to be placed on different parts of the knees superficially to find the optimal locations for maximizing signal quality. In addition, more subjects will be recruited for investigating how different loading and joint angle speed

on different rehabilitation exercises can impact the acoustical emissions using the AlterG and their importance in the rehabilitation process. The longitudinal measurements of cumulative joint loading forces in athletes or patients rehabilitating knee injuries may provide a means of assessing knee use during normal activities or exercises, which can then be provided to the user as feedback.

CHAPTER 4. QUANTIFYING ASYMMETRY BETWEEN MEDIAL AND LATERAL COMPARTMENT KNEE LOADING FORCES USING ACOUSTIC EMISSIONS

4.1 Introduction

Accordingly, an abnormally large knee joint load is considered an important factor in the development of OA [King]. Biomechanically, the medial knee compartment is the most susceptible to severe disease due to the natural alignment of the lower limb which places the ground reaction force directly through the medial compartment at a rate of 5-10 times that of the lateral compartment [10]. Quantifying the joint contact force (JCF) distribution or asymmetry between the medial and lateral compartments would provide important insights to understanding the relationship between JCF and potential progression of these pathologies. Musculoskeletal models (MSKM) are considered the current gold standard for estimating muscle forces and JCF and these models have been used in the literature to estimate tibiofemoral JCF [53]. Although this is a non-invasive method, it is limited to a controlled lab setting requiring motion capture cameras for joint angles, force plates for ground reaction force (GRF) and electromyography (EMG) sensors for muscle activation making it difficult to monitor and measure joint loading outside of lab environments.

In this chapter, we present a novel approach using representation learning, specifically convolutional autoencoders (CAE), to learn the compressed representation of the joint acoustic emissions to build a subject independent model that can estimate the

directional bias of joint load asymmetry between medial and lateral compartments of the knee and generalize to new and unseen subjects. We hypothesize that time-frequency representation of the acoustic signal and a multi-sensor fusion technique can improve the performance of the subject independent classification model over the handcrafted features. Previous study has used short time Fourier transform (STFT) of knee acoustic signals to classify healthy versus injured knee [54]. In this work, we further investigate different types of time-frequency representation known as scalogram using three different wavelet transforms. Different types of fusion are explored such as signal level fusion which includes cross spectrogram and wavelet coherence prior to features extraction and feature level fusion which combines the two or more extracted features matrices into a single matrix either by concatenating or adding. We used a hybrid machine learning algorithm consisting of both neural networks and support vector machine (SVM) for classification and has shown for the first time that the medial to lateral load distribution can be quantified and that wavelet coherence yields the best performance.

4.2 Materials and Methods

4.2.1 Study Participant

Sixteen able-bodied subjects (10 male / 6 female, age: 24.7 ± 3.6 years, height: 171 ± 7.5 cm, weight: 71 ± 10 kg) participated in this study under the approval from the Georgia Institute of Technology Institutional Review Board. Inclusion criteria included no history of major knee injury or surgery.

4.2.2 Hardware Setup and Data Acquisition

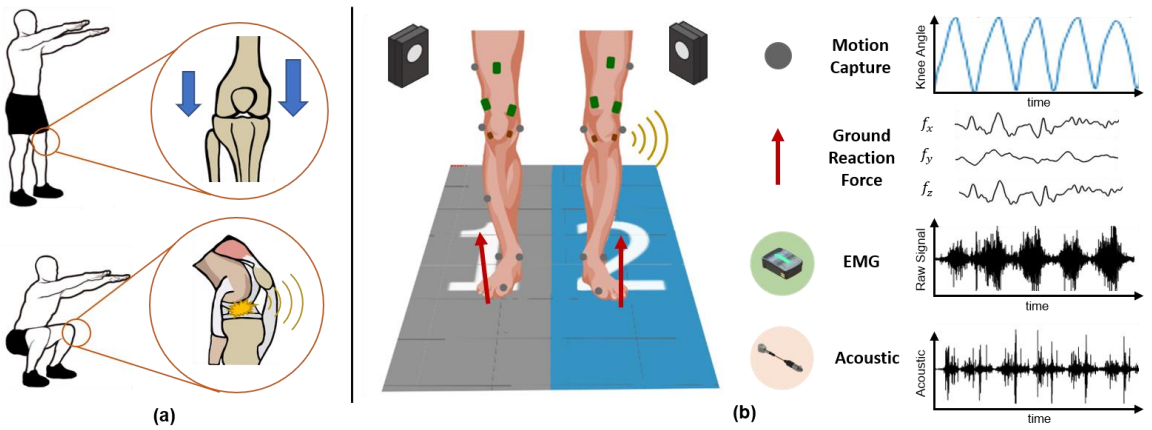

Figure 16. Experimental procedure and system architecture. (Left) Subject performing squat exercises. The knee joint acoustical emission could indicate the asymmetry in medial and lateral compartmental forces. (Right) Experimental setup including motion capture system to calculate the kinematics, electromyography sensors for muscle activation, force plate to detect ground reaction force, and contact microphones for acoustic detection from the knee joint.

Each subject was instrumented with 20 reflective body markers to provide full 3D kinematics of the subject's lower limbs based on the Plug-In Gait lower body mode [55]. These markers were tracked using a motion capture system including 15 infrared cameras at a sampling rate of 200 Hz (Vicon Motion Systems, Denver, CO, USA). The subject stood on force plates (Bertec, Columbus, OH, USA) to capture the GRF and center of pressure on each leg with a sampling rate of 1 kHz. Twelve EMG sensors (Trigno Wireless EMG, Delsys, Natick, MA) were placed on key muscles targeted during squat exercises on the left and right leg: namely, rectus femoris, vastus lateralis, vastus medialis, biceps femoris, semitendinosus and the lateral gastrocnemius [56]. Fig. 16a illustrates our hypothesis and Fig. 16b shows the measurement setup used to capture the necessary biomechanical signals to calculate JCF. Data collection took place in the biomechanics lab with the assistance in experimental setup and supply of materials from the members of Exoskeleton and Prosthetic Intelligent Controls Lab at Georgia Institute of Technology.

The acoustic emissions from the knee were captured using miniature, high-bandwidth, uniaxial accelerometers (series 3225, Dytran Instruments, Inc., Chatsworth, CA, USA) which have a high sensitivity (100mV/g), low noise floor (700 ugrms) and a broad bandwidth (up to 10 kHz). These accelerometers were attached to the medial and lateral sides of the patella tendon on both the left and right knees using adhesive tape. These locations have been used in previous studies as they provide the optimal contact area and minimize the influence of soft tissue, muscle, and fat on the acoustic signals [57]. These signals were collected with a sampling rate of 25 kHz using a data acquisition device (NI USB-4432, National Instruments Corporation, Austin, TX) through MATLAB software (MathWorks, Natick, MA).

4.2.3 Experimental Procedure

After being instrumented with these sensors, the subject was asked to perform 10 cycles of deep flexion squats across three different leg stances. The speed of the squat was controlled to 4 seconds per cycle using a metronome (2 seconds down, 2 seconds up) to mitigate the effect of velocity on the acoustic emissions. The baseline condition was defined as a squat with the feet at approximately the subject's shoulder-width apart and is considered the most common posture for the subjects when performing a squat movement. A narrow squat was defined as a squat with the leg stance width less than half of the baseline condition and the wide squat was defined as a squat with the leg stance approximately twice as big as the baseline condition. Previous studies showed that the shear force was much greater in narrow stance squat than shoulder-width or wide stance [58] and that the increasing stance width resulted in the center of pressure being placed more on the lateral side [59]. Thus, these two conditions (narrow and wide stance widths)

were expected to change the loading on the medial and lateral compartments of the knee thus creating a larger asymmetry compared to the baseline condition.

4.2.4 Joint Contact Force Estimation

The marker trajectory data, GRF, and EMG signals were filtered and processed with a MATLAB toolbox MotoNMS [60] and were used as an input to the musculoskeletal modeling software called OpenSim [61]. To calculate the JCF in the medial and the lateral compartments of the knee during squats, a custom MSKM designed by Bedo et. al. was implemented [62]. This model is a modified version from the generic model that computes the medial and lateral tibiofemoral contact force by resolving the differences between the two using the tibial and femoral components and allowing larger lower-limb range of motion. This MSKM was scaled for each subject and the joint angle (inverse kinematics), joint moments (inverse dynamics), and muscle moment arms (muscle analysis) were derived from the OpenSim. Muscle forces were computed using the Calibrated EMG-Informed Neuromusculoskeletal Modelling Toolbox (CEINMS) [63]. This toolbox comprises EMG-assisted algorithms that adjusts existing excitations from experimental EMG signals and uses static optimization to synthesize the muscle activations for muscles that were not collected experimentally. Using these muscle forces along with joint moments and internal and external loads, the medial and lateral JCF were derived using the JointReaction analysis and were segmented for each squat cycle. The resultant forces were normalized to each subject's BW.

4.3 Joint Acoustic Emission Processing

4.3.1 Handcrafted Features

The acoustic signals were downsampled and bandpass filtered between 10 Hz to 2 kHz. Although the frequency band of the sensors and filtering cut-off frequencies differ in the literature, this frequency bandwidth was chosen based on previous studies [64][65] as this range contains both the lower frequency grinding loudness and the large-amplitude, short-duration clicks of the acoustic signals while removing the baseline wanders caused by the limb movement. After preprocessing, the filtered data was segmented into each squat cycle and the most widely used features such as spatiotemporal, spectral, Mel-frequency cepstrum coefficient, and gammatone cepstral coefficients were extracted with 100ms window size and 50% overlap. For each squat cycle, the average and standard deviation of these windowed features were calculated to provide a single instance.

4.3.2 Audio-to-Image Representation

In this work, we explored four types of image representation of the acoustic signals. The spectrogram is a time-frequency representation of the acoustic signal generated by STFT [66] with a hamming window of size 50ms with 50% overlap. The power spectrogram which is the square magnitude of the complex-valued amplitude spectrogram is the most common representation as it is easily interpretable. The scalogram is the time-frequency representation of the acoustic signal generated by a wavelet transformation [67]. There are three different types of wavelets used in this study: morse which is useful for analyzing signals with time-varying amplitude and frequency [68], Morlet which has equal variance in time and frequency [69], and bump which has wider variance in time and narrower variance in frequency [70]. Given a time series signal $x(t)$, a continuous wavelet transform can be expressed as follows:

$$W_x(u,s) = \frac{1}{\sqrt{s}} \sum_{-\infty}^{+\infty} x(t) \psi^* \left(\frac{t-u}{s} \right) \quad \text{(x)}$$

where ψ represents a Fourier transform of designated wavelet, s denotes the scale factor, u represents time shift factor and * denotes a complex conjugate.

These time-frequency representation are expressed in two-dimensional matrix using the aforementioned calculation of spectrograms and/or scalograms. STFT provides uniform time-frequency resolution and wavelet transformation yields better time localization at higher frequencies and better frequency localization at lower frequencies than the spectrogram [71].

4.3.3 Sensor Fusion Methods

Sensor fusion is a technique of combining multiple signals from multiple sensors to extract more useful information than the ones provided by the single sensor. Two types of fusion mechanisms are explored in this work: signal-level fusion and feature-level fusion. Signal-level fusion refers to the combination of signals from the multiple sensors. In this case, the relationship of the two signals is extracted and used as an input to the CAE. The sampling rate, data size and time synchronization should be comparable between the multiple signals. This method computes correlation between two acoustic signals prior to the feature extraction. One approach is the cross spectrogram which is a cross-correlation in the frequency domain between the two signals [72]. Given two time series x and y, the cross spectrum Γ_{xy} can be expressed as follows:

$$\Gamma_{xy} = \mathcal{F}\{\gamma_{xy}\}(f) = \sum_{\tau=\infty}^{\infty} \gamma_{xy}(\tau) e^{-2\pi i \tau f} \quad \text{(x)}$$

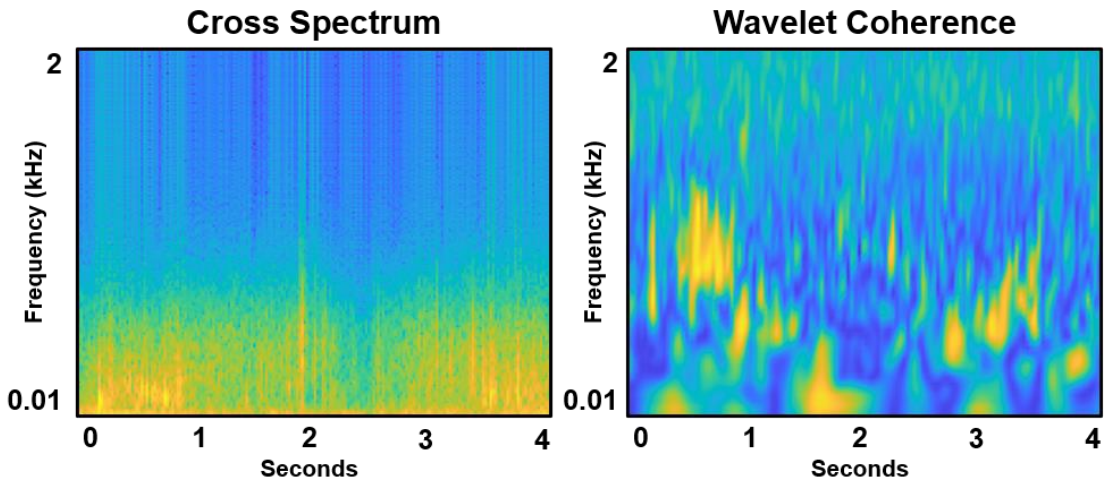

Figure 16. Example of a cross spectrum and wavelet coherence of the acoustic signal for a single squat cycle.

where γ_{xy} is the cross-variance function and $\mathcal{F}$ is the Fourier transform. The log-magnitude can be calculated from this equation to provide the 2-D input to our CAE. The other approach is the magnitude-squared wavelet coherence. The wavelet coherence is computed using the Morlet wavelet over logarithmic scales [73]. Given two time-series signals $x(t)$ and $y(t)$,wavelet coherence can be expressed as following:

$$Wcoh(u,s) = \frac{\left|S\left(W_x^*(u,s)W_y(u,s)\right)\right|^2}{S(|W_x(u,s)|^2)\cdot S(\left|W_y(u,s)\right|^2)} \quad \text{(x)}$$

where $W_x(u,s)$ and $W_y(u,s)$ denote the continuous wavelet transforms of $x(t)$ and $y(t)$ at scales u and time shift factor s. S is a smoothing function in time and scale domain that keeps the balance between frequency resolution and significance. Fig. 17 visually represents the differences between the two signal level fusion methods. In feature-level fusion, the fusion occurs after the features are extracted from each sensor. The most common method is fusing the features extracted individually from the autoencoder by

concatenating the two feature spaces together [74]. We will compare the performance of the different sensor fusion methods to determine the robustness of using multi-sensor approach and to define which sensor fusion methods best estimate the directional bias of asymmetry between medial and lateral compartment JCF.

4.4 Representation Learning for Feature Extraction

4.4.1 Convolutional Neural Network

A convolutional neural network (CNN) is a widely used deep learning algorithms successfully applied in fields of computer vision. The benefit of CNN is that it can successfully capture the spatial information of the input image data without losing important features when the image is flattened to a single vector as an input [75]. CNN consists of convolutional layer, and a pooling layer. Convolution layer is where the convolution operation occurs that involves multiplication of a set of weights with the input to extract comprehensive features of the input image. This multiplication is performed between the input data and a 2-D array of weights determined by the kernel size. Usually, the first convolutional layer captures the low-level features such as edges, color, and gradient orientations. With more layers, the architecture will learn the high-level features that gives an overall understanding of the input data. There are other parameters to consider when formulating the convolutional layer: number of filters, padding, and activation. Number of filters can be understood as number of feature detectors that the network can potentially learn. Activation function such as rectified linear unit (ReLU) helps to decide whether to activate the neurons or not. Padding is used to handle the problem of preserving the information at the border by filling a layer of zeros around the input image [76].

The pooling layer is optional but is widely used in CNN to reduce the spatial size of the convolved feature to decrease the computational power required to process the data and to extract dominant features of the image. In general, there are two types of pooling: max pooling and average pooling. Max pooling takes the maximum value within a matrix while the average pooling computes the average value. In this work, we employed max pooling which is known to contain more informative features and improves generalization performance [77].

4.4.2 Convolutional Autoencoder

An autoencoder is a self-supervised neural network model that learns the compressed representation of the input data and tries to reproduce the input at the output [78]. Autoencoder consists of two parts: an encoder that learns the informative features of the input and compresses it into a latent space; a decoder that tries to reconstruct the input from the compressed representation provided by the encoder. Given a set of input data $X = \{x^{(1)}, x^{(2)}, x^{(3)}, \cdots\}$, where $x^{(i)} \in R^n$, the encoder can be represented as $\varphi: x \in X \rightarrow h \in D$ where the function φ maps the input data X to latent space D. The decoder can be represented as $\psi: h \in D \rightarrow x' \in X$ where the function ψ maps the latent space D to the output which is expected to be same as the input. Through the training process, the autoencoder applies backpropagation by taking the input data as the target variable (i.e., $y^{(i)} = x'^{(i)} = x^{(i)}$) and minimizes the reconstruction errors using the loss function such as mean squared error.

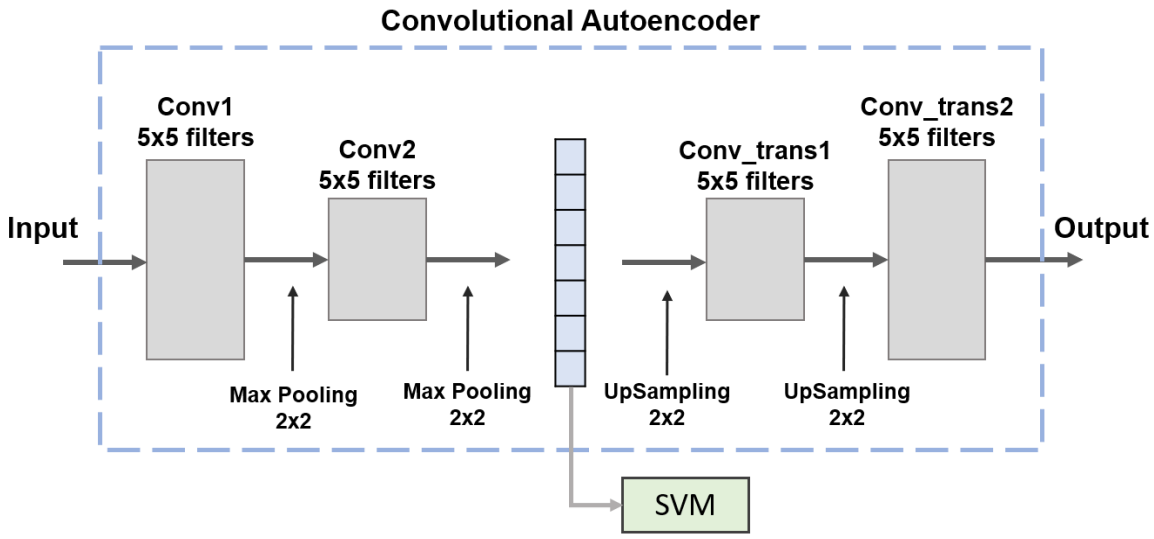

Figure 1817. Hybrid machine learning algorithm consisted of CAE and SVM. The encoder has two convolutional layers with kernel size of 5 and filter size of 10 and 20, respectively. Max pooling layer is added after each convolutional filter. The decoder has a similar layout as the encoder. Once CAE is trained, the encoder will extract the reduced representation of both training and testing data which is used as an input to the SVM classification model.

CAE is a variant of CNN where the encoder and decoder are basically a form of CNN [79]. The convolutional encoder extracts the important features to a feature map from the 2-D input, while the convolutional decoder reconstructs the feature map to the output.

4.4.3 Model Architecture

The proposed model used in this study is the CAE using a two-layer of CNN architecture for encoder and decoder individually and SVM for classification shown in Fig. 18. We used SVM as our classification model due to its ability to work with a smaller dataset and high dimensional space [80]. This hybrid machine learning algorithm consisting of both neural networks for feature extraction and SVM for classification task has commonly been used in other studies [81-83]. Since the dataset is relatively small, reducing the number of trainable parameters would help prevent overfitting. We employed

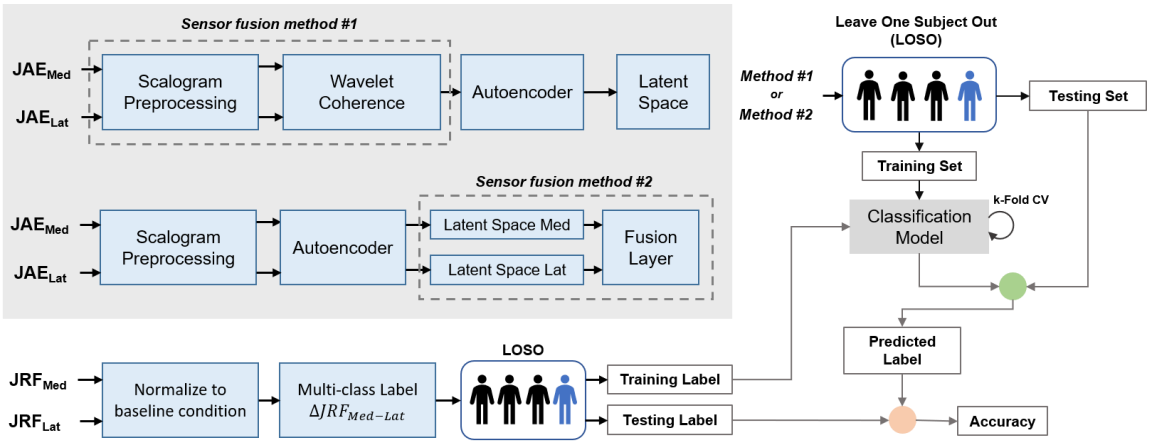

Figure 19. Overview of the signal processing with sensor fusion methods and machine learning pipeline.

a nested cross validation along with grid search to find the optimal hyperparameters for the autoencoder and the SVM [84] and the model parameters were kept the same to ensure that the model performance on an unseen subject can be evaluated fairly. Some of the hyperparameters that were tuned were the number of layers (1-3), number of filters (10-60, in increments of 10), kernel size (3,5,7), activation functions {tanh, ReLU, sigmoid}, and the optimizer in the set {Adadelta, RMSProp, Adam, stochastic gradient descent (SGD)}. The first convolutional layer consists for 10 filters, a kernel size of 5, a ReLU activation function, and a max pooling. The second convolutional layer is similar except the number of filter is increased to 20. For the model training, we used mean squared error (MSE) as the loss function and 200 epochs with an early stopping to prevent overfitting [85] if the validation loss did not continue to decrease in 5 epochs. Once the CAE is trained, the decoder is discarded, and the encoder is used as a feature extractor to obtain the reduced dimension of the input data. The model's performance was tested using the leave-one-subject-out cross validation (LOSO-CV) split where the model was trained and tuned using the 15 subject's data. The idea is to validate whether the model can predict on an unseen

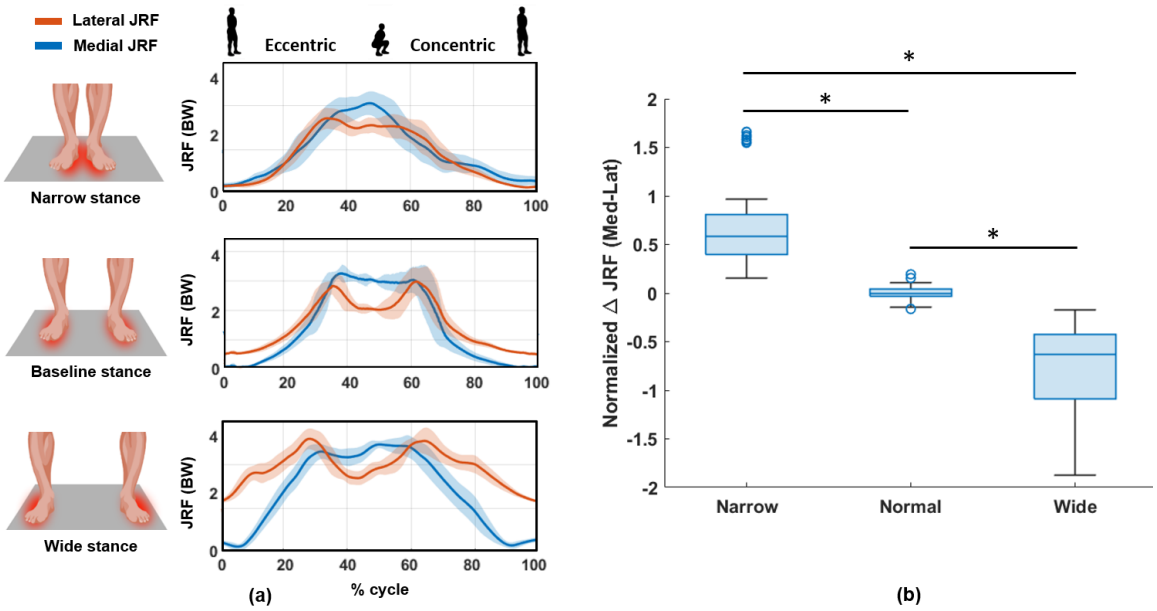

Figure 20. (a) Joint contact force for medial and lateral side for three different conditions. The joint contact force per cycle was calculated as the area under the curve which indicates the overall force acting on the knee joint per squat cycle. (b) Boxplot showing statistical difference among three conditions.

data recurrently. The LOSO train-test split was performed such that all subject's data was tested once and the accuracy of the model for each subject was averaged. The F1 score, precision and recall were also reported to provide insights to performance of the model. The overall pipeline is illustrated in Fig. 19.

4.5 Results and Discussion

4.5.1 Joint Contact Force Analysis

The overall JCF of the medial and lateral compartment were normalized to their baseline condition and the difference (ΔJRF) between the two were calculated for each squat cycle. In general, the peak compressive force at the medial side was higher than the lateral side for a shoulder-width baseline squat. Fig. 20a illustrates an example of the averaged medial and lateral JCF of a single subject for each squat condition. In general,

Table 3. Sensor Fusion Classification Accuracy on Unseen Subject (%)

Feature-Level		Signal-Level	
Spectrogram	51.7 ± 3.4 %	Cross-spectrum	75.49 ± 6.8%
Morse	67.6 ± 2.8%	Wavelet	83.75 ± 6.3%
Bump	63.4 ± 8.7%		
Morlet	69.9 ± 4.2%		

the normalized ΔJRF showed that certain ranges ($|\Delta JRF| < 0.1BW$) can be referred to as a baseline or no asymmetry. The actual value of medial and lateral JCF will not be the same and the difference between the two will be different from subject to subject. Thus, to define asymmetry, this baseline range is considered as having no imbalance between the medial

and lateral JCF. The medial JCF was higher than the lateral JCF for narrow squat condition ($\Delta JRF > 0.1BW$) and vice versa for the wide squat condition ($\Delta JRF < -0.1BW$). We validated the statistical significance between these three conditions using a Wilcoxon signed rank test [86] across subjects and showed that these three conditions were statistically significant from one another. Bonferroni correction was applied for multiple comparison [87]. Fig. 20b demonstrates boxplot for the normalized ΔJRF for each condition across all subjects. The purpose of these different experimental conditions was to introduce an extreme case that would cause the medial JCF to be much greater than the later JCF and vice versa. The goal is to determine whether the joint acoustic emissions can detect these extreme conditions which are defined as greater than the assigned range of the baseline (-0.1 BW to 0.1 BW).

Table 4. Wavelet Coherence Precision, Recall, and F1-Score (%)

	Precision	Recall	F1-score
Narrow squat	78.77	86.52	77.21
Normal squat	93.61	90.53	91.73
Wide squat	87.01	86.46	85.15

4.5.2 Using CAE for Feature Extraction

The comparison of the time frequency representations of a single sensor (medial and lateral) and the feature-level fusion method is shown in Table 3. The results showed that for the feature-fusion method, the Morlet wavelet had the highest accuracy of 69.9 ± 4.2%. The cross-spectrum method shows an accuracy of 75.49 ± 6.8% while the wavelet coherence shows an accuracy of 83.76 ± 6.3%.

These results indicate that using the signal-level fusion of wavelet coherence yielded the highest accuracy of estimating the direction of medio-lateral joint distribution which suggests that the difference in the medial and lateral compartment JCF can be best described as the wavelet coherence between the acoustic signals captured from the medial and lateral side of the patella. Table 4 shows the precision, recall and F1-score of the testing set using the wavelet coherence for all the squat conditions. This indicates that the model's accuracy on the testing set is not skewed to one condition and that the model performed consistently well across subjects and across conditions.

4.5.3 Handcrafted versus Automated Features

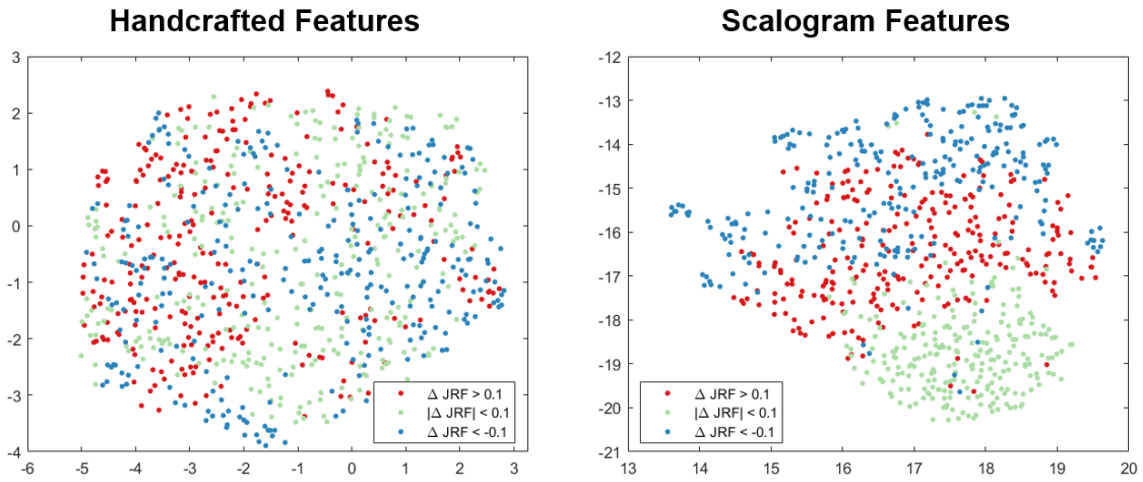

Figure 18. Comparison of the unsupervised clustering of the acoustic signal for different conditions.

We also explored the performance of the handcrafted features and compared them with the automated features from the CAE. Fig. 21 shows the comparison of these two feature extraction methods using a uniform manifold approximation and projection (UMAP) which is a dimensionality reduction technique used for visualization that can take in non-linear dimensions and preserves more of the global structure with faster run time [88]. Automated features extracted from the wavelet coherence between two signals were used as an input to this dimensionality reduction technique. This visualization indicates that the handcrafted features show much overlap between the squat conditions while the automated features relatively show some separation which is also shown in the aforementioned testing accuracy result. We applied the same machine learning method using the handcrafted features to test the performance of the model on an unseen subject's data. The handcrafted features extracted from medial and lateral sensors were concatenated into a single matrix where the rows represent each cycles and columns represent features.

To improve the performance of the model and reduce high structural variability of the knee between subjects, forward feature selection was implemented to select most discriminative and less subject-specific features. Once the generalizable features have been selected, the SVM was trained with LOSO-CV. The testing accuracy across subjects came out to be $47.63 \pm 7.8\%$ which demonstrates that these handcrafted features may not generalize across all subjects

4.5.4 Discussion

This is the first study to identify the direction of the medial and lateral load distribution of the knee joints using acoustic emissions. Previous studies attempted to estimate the medial and lateral contact force during shoulder-width squat by using electronic force transducers embedded in the total knee replacement [11], designing a load cell embedded instrumented knee prothesis [12], or using several total knee arthroplasty (TKA) designs on a cadaver leg model [89]. Although using these force sensors could be more accurate and a direct measurement of the medial and lateral contact forces, these methods would only be applicable to patients undergoing TKA treatments. Additionally, these studies recruited either a single subject with age greater than 70 or used cadaver leg models. Other studies investigated the effect of stance width during squats to understand how knee forces and muscle activation varies [90, 91]. Escamilla et al computed tibiofemoral contact force (TFCF) and demonstrated that TFCF were on average 15-16% higher in wide stance squat compared with the narrow stance squat [90]. Lorenzetti et al showed that the knee external moments, which has been studied as a potential measure of medial JCF [92, 93], was the highest in the narrow stance squat followed by the shoulder-width and the wide stance squat [91].

Since our method is not a direct measurement of the magnitude of medial and lateral contact forces, direct comparison of this method to previous literatures cannot be made. However, the MSKM used in this study demonstrated that in the shoulder-width squat, the medial compartment JCF were generally higher than the lateral across the subjects (medial to lateral load ratio = 1.1 ± 0.5) and the ratio between the medial and lateral JCF was higher in narrow stance squat than the wide stance squat (medial to lateral load ratio for narrow squat = 1.5 ± 0.4, medial to lateral load ratio for wide squat = 0.8 ± 0.3).

4.6 Conclusion and Future Work

These preliminary findings demonstrate that joint acoustic emissions can be used as a potential measure to detect the internal medio-lateral asymmetry of knee joint force. There are a few limitations in this study. One limitation is that the model does not estimate the actual magnitude difference of the JCF for the three squat exercises. The results from MSKM modeling showed that varying leg stance width while squatting showed a statistically significant difference of the medial and lateral JCF. While the normalized ΔJRFs for baseline squat relatively fall within the range between -0.1 BW and 0.1 BW, the absolute value of other conditions can vary from as little as 0.2 BW up to 4.6 BW. Further research is needed to estimate the actual difference of the medial and lateral JCF or the quantitative magnitude of JCF on each side. Also, knowledge of actual medial and lateral JCF would provide further insight to clinicians and patients allowing them to monitor knee compartment loading over time, therefore enabling more informed treatment decisions. Another limitation is that only one type of activity was explored in this study. It is expected that the characteristics of the joint acoustic emissions would differ based on the range of motion. Further research should investigate the medial to lateral load distributions for

different types of activities such as stair climbing, standing-up, sitting-down, and walking which is considered the most common activity of daily living.

In this chapter, we have demonstrated for the first time that joint acoustic emissions can be used to determine the imbalance or asymmetry between the medial and lateral compartment joint contact forces during squats. We developed a novel method of interpreting the signals from sensors attached to the medial and lateral side of the patella tendon by using a wavelet coherence and learning compressed representation of this coherence using a convolutional autoencoder. Results demonstrate that acoustic emissions can be used to determine the directional bias of medial to lateral load distribution and that acoustic signals can be used to determine the medio-lateral asymmetry on an unseen subject's data. These findings suggest the possibility of using wearable devices to measure joint sounds and monitor the medial to lateral joint load distribution without the need to collect biomechanical data in the laboratory environment. Wearable sensing technology to quantify medial to lateral joint load distribution would have clinical values as well since over usage of knee loads can potentially lead to osteoarthritis, especially on the medial side. This wearable technology would also provide useful insights on determining appropriate exercises for rehabilitation and treatment without overloading a specific compartment within the knee.

CHAPTER 5. CONCLUSION AND FUTURE WORK

5.1 Conclusion

This work presents algorithms that can be used for longitudinal joint health assessment. The ultimate vision of this work is to allow users to monitor their joint health outside of clinics and laboratory settings and receive feedback throughout their daily activities, ideally in the form of a wearable system. JAEs can serve as a potential biomarker to quantify joint health as the sensors and systems to capture these signals can be designed to be wearable.

In this dissertation, key scientific findings helped pave the way towards enabling longitudinal joint health monitoring using JAEs. As a first step, we developed a novel method for processing JAE by investigating the knee sounds recorded from athletes at the time of an acute injury and 4-6 months of post recovery. We validated that the *b*-value of the acoustic signals can quantify changes in the knee health for patients with acute injuries and throughout rehabilitation. We further validated this novel method by exploring the cadaver model of acute knee injury and the changes before and after injury. This method of using the *b*-value greatly enhances the potential for incorporating a joint sound detection suite into a wearable system by allowing the device to be equally as effective in tracking rehabilitation improvement of the knee following acute injury while requiring far less computational time and power.

One of the important parameters for understanding joint health is quantifying the overuse and changes of knee joint loads in activities of daily life. In this dissertation, the

relationship between the changes in increasing mechanical stress and the JAEs is quantified by using an unsupervised graph mining algorithm that determines the number of complex communities within the signal. As the knee joint experienced greater loads, the number of communities increased accordingly, suggesting that JAE can be leveraged as a biomarker for detecting changes in knee joint load. In addition, we quantified the directional bias of medial to lateral load distribution from JAEs by using sensor fusion and hybrid machine learning algorithm in a subject independent model. There is no gold standard set of handcrafted features that can explain the conditions of the knee health and the importance of the features differ from subject to subject. The ability to overcome subject variability by using automated feature extraction method shows the potential that JAEs can be used to quantify JCF in diverse activities without the need to collect biomechanics data in a lab.

5.2 Future Directions

There are several future research directions from this work. First, further clinical studies can be conducted to collect a broad range of data with diverse injury types of the knee along with multiple recordings throughout the days or weeks following the injuries as the patients complete rehabilitation. In addition, other demographic information or clinical data can be simultaneously collected that defines the health of the knee. This could provide more insights and details as to how JAEs change as the joint starts to heal and return to the healthy status. This could also lead to improved signal processing methods that are more intuitive and effective that can be incorporated in a wearable sensing system.

Second, future work towards conducting studies to quantify the usage of the knee and measure knee joint load in everyday activities could broaden the scope of joint health

assessment. Most of the previous studies in clinics have recorded JAE through a simple motion, namely flexion extension and sit-to-stand (or squat) as these maneuvers allow more controlled and repeatable measures. Exploring other common activities such as walking and stair climbing, or rehabilitation exercises such as leg press and step ups could augment the datasets for understanding biomechanical and physiological changes of the knee joint using JAEs and how they change as the patients undergo rehabilitation. Furthermore, methods to process JAEs that can overcome subject variability across multiple activities should be investigated. The goal of using JAEs is to allow users to measure joint health outside of labs or clinics. Further research should examine robust feature extraction methods that would allow users to assess their knee usage in any activities without the need to take measurements in the biomechanics lab.

Finally, future work should involve determining the number of sensors and investigating more effective signal processing methods that would provide best performance using a wearable device. Current studies are mostly confined to a controlled setting such as in the clinic or in the biomechanics lab. The hardware and sensor modality in a wearable mechanism could be more uncontrolled including loose contact or wire interference during more dynamic activities such as walking and stair climbing. Signal processing methods that effectively handles these artifacts should be integrated to collect high quality and useful data.

5.3 Aspirations and Potential Impact of This Work

With rising healthcare cost and advancement in artificial intelligence driven technologies, remote health monitoring provides a promising alternative to clinical visits

and could benefit many patients by saving time and cost. Especially in joint health monitoring, the current gold standard tools such as MRI, X-rays, and CT scans are not well-suited for longitudinal measurement throughout days or weeks as they are time-consuming, costly, and limited to clinical settings. A wearable sensing technology, specifically using a novel sensing modality such as joint acoustics, could reveal information regarding the underlying joint structure or quantify complex biomechanical parameters that would previously need to be measured either in clinics or laboratory settings. For instance, joint load is a force applied to a weight-bearing joint where abnormal knee loading can lead to different types of injuries or conditions such as OA. An appropriate amount of knee loading is important to build durable cartilage while proper unloading is needed to allow healing and repair of the tissues. An ability to measure the mechanical stress on the knee using a wearable measurement of joint sounds could allow patients to monitor their knee daily and provide insights to the progression of OA and other types of diseases.

This dissertation explored whether wearable JAEs measurements can be used as a potential biomarker for longitudinal joint health assessment and for the first time investigated whether knee joint loads can be quantified using these sounds. The adverse effects of joint health from the structural change to loading are common and represent such a large component of healthcare expenses. We envision that our efforts will eventually reach and benefit many people in need to readily assess their joint health anytime and anywhere and provide longitudinal monitoring capability.

REFERENCES

[1] A. A. o. O. Surgeons, "Information About Musculoskeletal Conditions," *Disponibile da*, 2013.

[2] T. A. Blackburn and E. Craig, "Knee anatomy: a brief review," *Phys Ther*, vol. 60, no. 12, pp. 1556-60, Dec 1980, doi: 10.1093/ptj/60.12.1556.

[3] M. Majewski, H. Susanne, and S. Klaus, "Epidemiology of athletic knee injuries: A 10-year study," *Knee*, vol. 13, no. 3, pp. 184-8, Jun 2006, doi: 10.1016/j.knee.2006.01.005.

[4] H. J. Braun and G. E. Gold, "Diagnosis of osteoarthritis: imaging," *Bone*, vol. 51, no. 2, pp. 278-88, Aug 2012, doi: 10.1016/j.bone.2011.11.019.

[5] C. Reinschmidt, A. J. van den Bogert, B. M. Nigg, A. Lundberg, and N. Murphy, "Effect of skin movement on the analysis of skeletal knee joint motion during running," *J Biomech*, vol. 30, no. 7, pp. 729-32, Jul 1997, doi: 10.1016/s0021-9290(97)00001-8.

[6] G. Y. el-Khoury, M. H. Kathol, and W. W. Daniel, "Imaging of acute injuries of the cervical spine: value of plain radiography, CT, and MR imaging," *AJR Am J Roentgenol*, vol. 164, no. 1, pp. 43-50, Jan 1995, doi: 10.2214/ajr.164.1.7998567.

[7] W. Blodgett, "Auscultation of the knee joint " *Boston Medical and Surgery Journal*, vol. 146, no. 3, pp. 63-6, January 16 1902.

[8] L. K. Shark, H. Chen, and J. Goodacre, "Discovering differences in acoustic emission between healthy and osteoarthritic knees using a four-phase model of sit-stand-sit movements," *Open Med Inform J*, vol. 4, pp. 116-25, Jul 27 2010, doi: 10.2174/1874431101004010116.

[9] J. Prior *et al.*, "Analysis of high frequency acoustic emission signals as a new approach for assessing knee osteoarthritis," *Ann Rheum Dis*, vol. 69, no. 5, pp. 929-30, May 2010, doi: 10.1136/ard.2009.112599.

[10] D. D. D'Lima, B. J. Fregly, S. Patil, N. Steklov, and C. W. Colwell, Jr., "Knee joint forces: prediction, measurement, and significance," *Proc Inst Mech Eng H*, vol. 226, no. 2, pp. 95-102, Feb 2012, doi: 10.1177/0954411911433372.

[11] Y. Jung, Y.-j. Koo, and S. Koo, "Simultaneous estimation of ground reaction force and knee contact force during walking and squatting," *International Journal of Precision Engineering and Manufacturing*, vol. 18, no. 9, pp. 1263-1268, 2017.

[12] A. Mündermann, C. O. Dyrby, D. D. D'Lima, C. W. Colwell Jr, and T. P. Andriacchi, "In vivo knee loading characteristics during activities of daily living as measured by an instrumented total knee replacement," *Journal of Orthopaedic Research,* vol. 26, no. 9, pp. 1167-1172, 2008.

[13] M. Cross *et al.*, "The global burden of hip and knee osteoarthritis: estimates from the global burden of disease 2010 study," *Ann Rheum Dis,* vol. 73, no. 7, pp. 1323-30, Jul 2014, doi: 10.1136/annrheumdis-2013-204763.

[14] K. P. Pritzker *et al.*, "Osteoarthritis cartilage histopathology: grading and staging," *Osteoarthritis Cartilage,* vol. 14, no. 1, pp. 13-29, Jan 2006, doi: 10.1016/j.joca.2005.07.014.

[15] R. M. Rangayyan and Y. F. Wu, "Screening of knee-joint vibroarthrographic signals using statistical parameters and radial basis functions," *Med Biol Eng Comput,* vol. 46, no. 3, pp. 223-32, Mar 2008, doi: 10.1007/s11517-007-0278-7.

[16] S. Cai, S. Yang, F. Zheng, M. Lu, Y. Wu, and S. Krishnan, "Knee joint vibration signal analysis with matching pursuit decomposition and dynamic weighted classifier fusion," *Comput Math Methods Med,* vol. 2013, p. 904267, 2013, doi: 10.1155/2013/904267.

[17] J. H. Lee, C. C. Jiang, and T. T. Yuan, "Vibration arthrometry in patients with knee joint disorders," *IEEE Trans Biomed Eng,* vol. 47, no. 8, pp. 1131-3, Aug 2000, doi: 10.1109/10.855942.

[18] Y. Shen, R. M. Rangayyan, G. D. Bell, C. B. Frank, Y. T. Zhang, and K. O. Ladly, "Localization of knee joint cartilage pathology by multichannel vibroarthrography," *Med Eng Phys,* vol. 17, no. 8, pp. 583-94, Dec 1995, doi: 10.1016/1350-4533(95)00013-d.

[19] H. M. Bassiouni, M. El-Deeb, N. Kenawy, E. Abdul-Azim, and M. Khairy, "Phonoarthrography, musculoskeletal ultrasonography, and biochemical biomarkers for the evaluation of knee cartilage in osteoarthritis," *Mod Rheumatol,* vol. 21, no. 5, pp. 500-8, Oct 2011, doi: 10.1007/s10165-011-0441-8.

[20] B. Mascaro, J. Prior, L. K. Shark, J. Selfe, P. Cole, and J. Goodacre, "Exploratory study of a non-invasive method based on acoustic emission for assessing the dynamic integrity of knee joints," *Med Eng Phys,* vol. 31, no. 8, pp. 1013-22, Oct 2009, doi: 10.1016/j.medengphy.2009.06.007.

[21] K. S. Kim, J. H. Seo, J. U. Kang, and C. G. Song, "An enhanced algorithm for knee joint sound classification using feature extraction based on time-frequency analysis," *Comput Methods Programs Biomed,* vol. 94, no. 2, pp. 198-206, May 2009, doi: 10.1016/j.cmpb.2008.12.012.

[22] B. Gutenberg and C. F. Richter, *Seismicity of the earth and associated phenomena,* 2d ed. New York,: Hafner Pub. Co., 1965, pp. ix, 310 p.

[23] S. T., Y. S., L. Z. W., and O. M., "Applications of the AE improved b-value to qualitative evaluation of fracture process in concrete materials," *Journal of Acoustic Emission,* vol. 19, pp. 118-132, 2001.

[24] S. T. F. K., A. T., and A. K., "Evaluation of progressive failure using AE sources and improved b-value on slope model tests," *Progress in Acoustic Emission,* vol. VII, pp. 529-534, 1994.

[25] B. S., "Suppression of Acoustic Noise in Speech Using Spectral Subtraction," *IEEE Transactions on Acoustics, Speech, and Signal Processing,* vol. ASSP-27, no. 2, 1979.

[26] S. Hersek *et al.*, "Acoustical Emission Analysis by Unsupervised Graph Mining: A Novel Biomarker of Knee Health Status," *IEEE Trans Biomed Eng,* vol. 65, no. 6, pp. 1291-1300, Jun 2018, doi: 10.1109/TBME.2017.2743562.

[27] H. K. Jeong, D. Whittingslow, and O. T. Inan, "b-Value: A Potential Biomarker for Assessing Knee-Joint Health Using Acoustical Emission Sensing," *IEEE Sens Lett,* vol. 2, no. 4, Dec 2018, doi: 10.1109/LSENS.2018.2871981.

[28] S. Krishnan, R. M. Rangayyan, G. D. Bell, and C. B. Frank, "Adaptive time-frequency analysis of knee joint vibroarthrographic signals for noninvasive screening of articular cartilage pathology," *IEEE Trans Biomed Eng,* vol. 47, no. 6, pp. 773-83, Jun 2000, doi: 10.1109/10.844228.

[29] M. J. Medvecky and F. R. Noyes, "Surgical approaches to the posteromedial and posterolateral aspects of the knee," *J Am Acad Orthop Surg,* vol. 13, no. 2, pp. 121-8, Mar-Apr 2005, doi: 10.5435/00124635-200503000-00005.

[30] W. R. Post, S. R. Akers, and V. Kish, "Load to failure of common meniscal repair techniques: effects of suture technique and suture material," *Arthroscopy,* vol. 13, no. 6, pp. 731-6, Dec 1997, doi: 10.1016/s0749-8063(97)90008-6.

[31] F. Guilak *et al.*, "The role of biomechanics and inflammation in cartilage injury and repair," *Clin Orthop Relat Res,* no. 423, pp. 17-26, Jun 2004, doi: 10.1097/01.blo.0000131233.83640.91.

[32] H. J. Kim, J. W. Fernandez, M. Akbarshahi, J. P. Walter, B. J. Fregly, and M. G. Pandy, "Evaluation of predicted knee-joint muscle forces during gait using an instrumented knee implant," *J Orthop Res,* vol. 27, no. 10, pp. 1326-31, Oct 2009, doi: 10.1002/jor.20876.

[33] C. D. J. and H. L. B., "Graph-based data mining," *IEEE Intelligent Systems & Their Applications,* vol. 15, no. 2, p. 32, Mar-Apr 2000.

[34] T. Giannakopoulos and A. Pikrakis, *Introduction to audio analysis: a MATLAB® approach*. Academic Press, 2014.

[35] R. Vergin, D. O'shaughnessy, and A. Farhat, "Generalized mel frequency cepstral coefficients for large-vocabulary speaker-independent continuous-speech recognition," *IEEE Transactions on speech and audio processing,* vol. 7, no. 5, pp. 525-532, 1999.

[36] J. J. Burred and A. Lerch, "A hierarchical approach to automatic musical genre classification," in *Proceedings of the 6th international conference on digital audio effects*, 2003: Citeseer, pp. 8-11.

[37] J. Hua, Z. Xiong, J. Lowey, E. Suh, and E. R. Dougherty, "Optimal number of features as a function of sample size for various classification rules," *Bioinformatics,* vol. 21, no. 8, pp. 1509-15, Apr 15 2005, doi: 10.1093/bioinformatics/bti171.

[38] J. Hua, Z. Xiong, J. Lowey, E. Suh, and E. R. Dougherty, "Optimal number of features as a function of sample size for various classification rules," *Bioinformatics,* vol. 21, no. 8, pp. 1509-1515, 2004.

[39] T. Hastie, R. Tibshirani, and J. Friedman, *The elements of statistical learning: data mining, inference, and prediction*. Springer Science & Business Media, 2009.

[40] L. Van der Maaten and G. Hinton, "Visualizing data using t-SNE," *Journal of machine learning research,* vol. 9, no. 11, 2008.

[41] A. Thomson, E. Einarsson, E. Witvrouw, and R. Whiteley, "Running speed increases plantar load more than per cent body weight on an AlterG® treadmill," *Journal of sports sciences,* vol. 35, no. 3, pp. 277-282, 2017.

[42] D. Xu, C. Shen, and F. Shen, "A robust particle filtering algorithm with non-Gaussian measurement noise using student-t distribution," *IEEE Signal Processing Letters,* vol. 21, no. 1, pp. 30-34, 2013.

[43] J. H. Levine *et al.*, "Data-driven phenotypic dissection of AML reveals progenitor-like cells that correlate with prognosis," *Cell,* vol. 162, no. 1, pp. 184-197, 2015.

[44] M. B. Pouyan and M. Nourani, "Clustering single-cell expression data using random forest graphs," *IEEE journal of biomedical and health informatics,* vol. 21, no. 4, pp. 1172-1181, 2016.

[45] P. F. Felzenszwalb and D. P. Huttenlocher, "Efficient graph-based image segmentation," *International journal of computer vision,* vol. 59, no. 2, pp. 167-181, 2004.

[46] E. Kosman and K. Leonard, "Similarity coefficients for molecular markers in studies of genetic relationships between individuals for haploid, diploid, and polyploid species," *Molecular ecology,* vol. 14, no. 2, pp. 415-424, 2005.

[47] F. D. Malliaros and M. Vazirgiannis, "Clustering and community detection in directed networks: A survey," *Physics Reports,* vol. 533, no. 4, pp. 95-142, 2013.

[48] M. Rosvall and C. T. Bergstrom, "Maps of random walks on complex networks reveal community structure," *Proceedings of the National Academy of Sciences,* vol. 105, no. 4, pp. 1118-1123, 2008.

[49] P. Cahan, H. Li, S. A. Morris, E. L. Da Rocha, G. Q. Daley, and J. J. Collins, "CellNet: network biology applied to stem cell engineering," *Cell,* vol. 158, no. 4, pp. 903-915, 2014.

[50] M. E. Newman and M. Girvan, "Finding and evaluating community structure in networks," *Physical review E,* vol. 69, no. 2, p. 026113, 2004.

[51] R. Gallager, "Variations on a theme by Huffman," *IEEE Transactions on Information Theory,* vol. 24, no. 6, pp. 668-674, 1978.

[52] H. P. Kriegel, P. Kröger, J. Sander, and A. Zimek, "Density-based clustering," *Wiley Interdisciplinary Reviews: Data Mining and Knowledge Discovery,* vol. 1, no. 3, pp. 231-240, 2011.

[53] F. E. Zajac, R. R. Neptune, and S. A. Kautz, "Biomechanics and muscle coordination of human walking. Part I: introduction to concepts, power transfer, dynamics and simulations," *Gait Posture,* vol. 16, no. 3, pp. 215-32, Dec 2002, doi: 10.1016/s0966-6362(02)00068-1.

[54] D. Kraft and G. Bieber, "Vibroarthrography using convolutional neural networks," presented at the Proceedings of the 13th ACM International Conference on PErvasive Technologies Related to Assistive Environments, Corfu, Greece, 2020. [Online]. Available: https://doi.org/10.1145/3389189.3397993.

[55] L. D. Duffell, N. Hope, and A. H. McGregor, "Comparison of kinematic and kinetic parameters calculated using a cluster-based model and Vicon's plug-in gait," *Proc Inst Mech Eng H,* vol. 228, no. 2, pp. 206-10, Feb 2014, doi: 10.1177/0954411913518747.

[56] G. K. Lenton *et al.*, "Tibiofemoral joint contact forces increase with load magnitude and walking speed but remain almost unchanged with different types of carried load," *PLoS One,* vol. 13, no. 11, p. e0206859, 2018, doi: 10.1371/journal.pone.0206859.

[57] D. C. Whittingslow, H. K. Jeong, V. G. Ganti, N. J. Kirkpatrick, G. F. Kogler, and O. T. Inan, "Acoustic Emissions as a Non-invasive Biomarker of the Structural Health of the Knee," *Ann Biomed Eng,* vol. 48, no. 1, pp. 225-235, Jan 2020, doi: 10.1007/s10439-019-02333-x.

[58] R. F. Escamilla, G. S. Fleisig, T. M. Lowry, S. W. Barrentine, and J. R. Andrews, "A three-dimensional biomechanical analysis of the squat during varying stance

widths," *Med Sci Sports Exerc,* vol. 33, no. 6, pp. 984-98, Jun 2001, doi: 10.1097/00005768-200106000-00019.

[59] Lee S., "Effects of Foot Placement on Resultant Joint Moments in the Lower Extremity Joints during the Squat," Ph.D. Ph.D. Dissertation, Department of Kinesiology, Texas Woman's University, Denton, Texas, 2015. [Online]. Available: https://twu-ir.tdl.org/bitstream/handle/11274/9959/2015LeeOCR.pdf?sequence=1

[60] A. Mantoan, C. Pizzolato, M. Sartori, Z. Sawacha, C. Cobelli, and M. Reggiani, "MOtoNMS: A MATLAB toolbox to process motion data for neuromusculoskeletal modeling and simulation," *Source Code Biol Med,* vol. 10, p. 12, 2015, doi: 10.1186/s13029-015-0044-4.

[61] A. Seth *et al.*, "OpenSim: Simulating musculoskeletal dynamics and neuromuscular control to study human and animal movement," *PLoS Comput Biol,* vol. 14, no. 7, p. e1006223, Jul 2018, doi: 10.1371/journal.pcbi.1006223.

[62] B. L. S. Bedo, D. S. Catelli, M. Lamontagne, and P. R. P. Santiago, "A custom musculoskeletal model for estimation of medial and lateral tibiofemoral contact forces during tasks with high knee and hip flexions," *Comput Methods Biomech Biomed Engin,* vol. 23, no. 10, pp. 658-663, Aug 2020, doi: 10.1080/10255842.2020.1757662.

[63] C. Pizzolato *et al.*, "CEINMS: A toolbox to investigate the influence of different neural control solutions on the prediction of muscle excitation and joint moments during dynamic motor tasks," *J Biomech,* vol. 48, no. 14, pp. 3929-36, Nov 5 2015, doi: 10.1016/j.jbiomech.2015.09.021.

[64] N. B. Bolus, H. K. Jeong, D. C. Whittingslow, and O. T. Inan, "A Glove-Based Form Factor for Collecting Joint Acoustic Emissions: Design and Validation," *Sensors (Basel),* vol. 19, no. 12, Jun 13 2019, doi: 10.3390/s19122683.

[65] S. Ota *et al.*, "Preliminary study of optimal measurement location on vibroarthrography for classification of patients with knee osteoarthritis," *J Phys Ther Sci,* vol. 28, no. 10, pp. 2904-2908, Oct 2016, doi: 10.1589/jpts.28.2904.

[66] L. Cohen, *Time-Frequency Analysis*. Englewood Cliffs, NJ: PrenticeHall, 1995.

[67] Qian, *Introduction to Time-Frequency and Wavelet Transform*. Upper Saddle River, New Jersey: Prentice-Hal, 2002.

[68] S. C. Olhede and A. T. Walden, "Generalized morse wavelets," *IEEE Transactions on Signal Processing,* vol. 50, pp. 2661-2670, 2002.

[69] J. Lin and L. Qu, "FEATURE EXTRACTION BASED ON MORLET WAVELET AND ITS APPLICATION FOR MECHANICAL FAULT DIAGNOSIS," *Journal of Sound and Vibration,* vol. 234, pp. 135-148, 2000.

[70] I. Daubechies, *Ten lectures on wavelets* (CBMS-NSF regional conference series in applied mathematics, no. 61). Philadelphia, Pa.: Society for Industrial and Applied Mathematics, 1992, pp. xix, 357 p.

[71] S. Lapins, D. C. Roman, J. Rougier, S. De Angelis, K. V. Cashman, and J. M. Kendall, "An examination of the continuous wavelet transform for volcano-seismic spectral analysis," *Journal of Volcanology and Geothermal Research,* vol. 389, p. 106728, 2020.

[72] H. v. Storch and F. W. Zwiers, *Statistical analysis in climate research*, 1st pbk. ed. Cambridge, UK ; New York: Cambridge University Press, 2001, pp. x, 484 p.

[73] A. Grinsted, J. C. Moore, and S. Jevrejeva, "Application of the cross wavelet transform and wavelet coherence to geophysical time series," *Nonlin. Processes Geophys.*, vol. 11, no. 5/6, pp. 561-566, 2004, doi: 10.5194/npg-11-561-2004.

[74] A. Khan, J. Sung, and J. Kang, "Multi-channel fusion convolutional neural network to classify syntactic anomaly from language-related ERP components," *Information Fusion,* vol. 52, pp. 53-61, 2019.

[75] J. Gu *et al.*, "Recent advances in convolutional neural networks," *Pattern Recognition,* vol. 77, pp. 354-377, 2018.

[76] A. Krizhevsky, I. Sutskever, and G. E. Hinton, "ImageNet Classification with Deep Convolutional Neural Networks," *Advances in Neural Information Processing Systems,* vol. 25, 2012.

[77] J. Nagi *et al.*, "Max-pooling convolutional neural networks for vision-based hand gesture recognition," *2011 IEEE International Conference on Signal and Image Processing Applications (ICSIPA)*, pp. 342-347, 2011.

[78] P. Vincent, H. Larochelle, I. Lajoie, Y. Bengio, and P. Manzagol, "Stacked Denoising Autoencoders: Learning Useful Representations in a Deep Network with a Local Denoising Criterion," *Journal of Machine Learning Research,* vol. 11, 2010.

[79] M. Chen, X. Shi, Y. Zhang, D. Wu, and M. Guizani, "Deep Features Learning for Medical Image Analysis with Convolutional Autoencoder Neural Network," *IEEE Transactions on Big Data,* 2017.

[80] R. Yu and M. Abdel-Aty, "Utilizing support vector machine in real-time crash risk evaluation," *Accid Anal Prev,* vol. 51, pp. 252-9, Mar 2013, doi: 10.1016/j.aap.2012.11.027.

[81] Z. Wang and Y.-J. Cha, "Unsupervised deep learning approach using a deep auto-encoder with an one-class support vector machine to detect structural damage," *Structural Health Monitoring,* p. 1475921720934051, 2020.

[82] M. Gutoski, N. M. R. Aquino, M. Ribeiro, E. Lazzaretti, and H. S. Lopes, "Detection of video anomalies using convolutional autoencoders and one-class support vector machines," in *XIII Brazilian Congress on Computational Intelligence*, 2017, vol. 2017: Rio das Ostras RJ.

[83] Y. Ju, J. Guo, and S. Liu, "A deep learning method combined sparse autoencoder with SVM," in *2015 international conference on cyber-enabled distributed computing and knowledge discovery*, 2015: IEEE, pp. 257-260.

[84] V. K. Ojha, A. Abrahan, and V. Snášel, "Metaheuristic design of feedforward neural networks: A review of two decades of research," *Engineering Applications of Artificial Intelligence,* vol. 60, pp. 97-116, 2017.

[85] L. Prechelt, "Automatic early stopping using cross validation: quantifying the criteria," *Neural Networks,* vol. 11, pp. 761-767, 1998.

[86] F. Wilcoxon, "Individual comparisons of grouped data by ranking methods," *J Econ Entomol,* vol. 39, p. 269, Apr 1946, doi: 10.1093/jee/39.2.269.

[87] R. A. Armstrong, "When to use the Bonferroni correction," *Ophthalmic Physiol Opt,* vol. 34, no. 5, pp. 502-8, Sep 2014, doi: 10.1111/opo.12131.

[88] E. Becht *et al.*, "Dimensionality reduction for visualizing single-cell data using UMAP," *Nat Biotechnol,* Dec 3 2018, doi: 10.1038/nbt.4314.

[89] B. Innocenti, S. Pianigiani, L. Labey, J. Victor, and J. Bellemans, "Contact forces in several TKA designs during squatting: a numerical sensitivity analysis," *Journal of biomechanics,* vol. 44, no. 8, pp. 1573-1581, 2011.

[90] R. F. ESCAMILLA *et al.*, "Effects of technique variations on knee biomechanics during the squat and leg press," *Medicine & Science in Sports & Exercise,* vol. 33, no. 9, pp. 1552-1566, 2001.

[91] S. Lorenzetti *et al.*, "How to squat? Effects of various stance widths, foot placement angles and level of experience on knee, hip and trunk motion and loading," *BMC Sports Science, Medicine and Rehabilitation,* vol. 10, no. 1, pp. 1-11, 2018.

[92] A. Trepczynski, I. Kutzner, G. Bergmann, W. R. Taylor, and M. O. Heller, "Modulation of the relationship between external knee adduction moments and medial joint contact forces across subjects and activities," *Arthritis & rheumatology,* vol. 66, no. 5, pp. 1218-1227, 2014.

[93] D. Zhao, S. A. Banks, K. H. Mitchell, D. D. D'Lima, C. W. Colwell Jr, and B. J. Fregly, "Correlation between the knee adduction torque and medial contact force for a variety of gait patterns," *Journal of orthopaedic research,* vol. 25, no. 6, pp. 789-797, 2007.